AGU PUBLICATIONS

Geochemistry, Geophysics, Geosystems

RESEARCH ARTICLE

10.1002/2016GC006655

Key Points:
- Joints, ductile shear zones, and faults formed in a cooling granodiorite pluton and preserve overprinting microstructures
- Synthesis of thermal model with microstructural data reveals timing of and potential relationships between structural events
- Uncertainty in TiO_2 activity and partial reequilibration during recrystallization limit utility of titanium-in-quartz thermobarometer

Supporting Information:
- Supporting Information S1
- Data Set S1
- Data Set S2

Correspondence to:
J. M. Nevitt,
jnevitt@usgs.gov

Citation:
Nevitt, J. M., J. M. Warren, S. Kidder, and D. D. Pollard (2017), Comparison of thermal modeling, microstructural analysis, and Ti-in-quartz thermobarometry to constrain the thermal history of a cooling pluton during deformation in the Mount Abbot Quadrangle, CA, *Geochem. Geophys. Geosyst.*, *18*, 1270–1297, doi:10.1002/2016GC006655.

Received 20 SEP 2016
Accepted 13 FEB 2017
Accepted article online 1 MAR 2017
Published online 30 MAR 2017

© 2017. American Geophysical Union. All Rights Reserved.

Comparison of thermal modeling, microstructural analysis, and Ti-in-quartz thermobarometry to constrain the thermal history of a cooling pluton during deformation in the Mount Abbot Quadrangle, CA

Johanna M. Nevitt[1,2], Jessica M. Warren[1,3], Steven Kidder[4], and David D. Pollard[1]

[1]Department of Geological Sciences, Stanford University, Stanford, California, USA, [2]Now at U.S. Geological Survey, Menlo Park, California, USA, [3]Now at Department of Geological Sciences, University of Delaware, Newark, Delaware, USA, [4]Department of Earth and Atmospheric Sciences, The City College of New York, New York, New York, USA

Abstract Granitic plutons commonly preserve evidence for jointing, faulting, and ductile fabric development during cooling. Constraining the spatial variation and temporal evolution of temperature during this deformation could facilitate an integrated analysis of heterogeneous deformation over multiple length-scales through time. Here, we constrain the evolving temperature of the Lake Edison granodiorite within the Mount Abbot Quadrangle (central Sierra Nevada, CA) during late Cretaceous deformation by combining microstructural analysis, titanium-in-quartz thermobarometry (TitaniQ), and thermal modeling. Microstructural and TitaniQ analyses were applied to 12 samples collected throughout the pluton, representative of either the penetrative "regional" fabric or the locally strong "fault-related" fabric. Overprinting textures and mineral assemblages indicate the temperature decreased from 400–500°C to <350°C during faulting. TitaniQ reveals consistently lower Ti concentrations for partially reset fault-related fabrics (average: 12 ± 4 ppm) than for regional fabrics (average: 31 ± 12 ppm), suggesting fault-related fabrics developed later, following a period of pluton cooling. Uncertainties, particularly in TiO_2 activity, significantly limit further quantitative thermal estimates using TitaniQ. In addition, we present a 1-D heat conduction model that suggests average pluton temperature decreased from 585°C at 85 Ma to 332°C at 79 Ma, consistent with radiometric age data for the field. Integrated with the model results, microstructural temperature constraints suggest faulting initiated by ~83 Ma, when the temperature was nearly uniform across the pluton. Thus, spatially heterogeneous deformation cannot be attributed to a persistent temperature gradient, but may be related to regional structures that develop in cooling plutons.

1. Introduction

Faults and ductile shear zones in crystalline rock often initiate due to reactivation of preexisting structures during cooling [e.g., joints, *Segall and Pollard*, 1983b; dikes, *Christiansen and Pollard*, 1997]. First analyzed in the Mount Abbot Quadrangle (central Sierra Nevada, CA) [*Lockwood and Lydon*, 1975; *Segall and Pollard*, 1983b], this interplay of brittle and ductile deformation has been recognized in a number of exhumed granitoid bodies, including the Adamello Batholith [southern Alps; e.g., *Pennacchioni*, 2005], the Neves region of the Tauern Window [eastern Alps; *Mancktelow and Pennacchioni*, 2005; *Pennacchioni and Mancktelow*, 2007], the Mont Blanc Massif [western Alps; e.g., *Guermani and Pennacchioni*, 1998], the Gran Paradiso nappe [northwestern Alps; *Menegon and Pennacchioni*, 2010], the Roses granodiorite [northeast Spain; *Segall and Simpson*, 1986], and the Mooshla pluton [Abitibi Belt, Canada; e.g., *Tourigny and Tremblay*, 1997]. The presence of pseudotachylyte associated with faults in these settings [e.g., *Di Toro and Pennacchioni*, 2004; *Griffith et al.*, 2008; *Pennacchioni and Mancktelow*, 2013] suggests seismic slip occurred, possibly producing earthquakes of magnitude 5.7 or greater [*Kirkpatrick et al.*, 2008]. Thus, investigating structural features in these settings benefits not only basic knowledge of how plutons accommodate deformation during cooling, but also assessment of seismic hazard associated with faults at evolving plate boundaries (e.g., magmatic arcs, suture zones).

The Mount Abbot Quadrangle has served as a natural laboratory for fundamental studies on a wide range of deformation processes in cooling plutons, including joint formation and interaction [e.g., *Segall and*

Pollard, 1983a]; mylonitic shear zone development [e.g., *Christiansen and Pollard*, 1997]; nucleation, interaction, and growth of strike-slip fault systems [e.g., *Segall and Pollard*, 1980, 1983b; *Martel et al*., 1988]; stress-dependent ductile fabric development [e.g., *Bürgmann and Pollard*, 1992, 1994]; and the occurrence of outcrop and kilometer-scale kink bands in granodiorite [*Davies and Pollard*, 1986; *Pachell et al*., 2003]. Many of these studies constructed mechanical models based on outcrop measurements and assessed modeling results relative to meso- and micro-structural interpretations of the natural features. However, the precise conditions (e.g., lithostatic pressure, *P*, and temperature, *T*) and timing of deformation, necessary to construct a unified tectonic model of the Mount Abbot Quadrangle, remain ambiguous [*Pennacchioni and Zucchi*, 2013]. Improved knowledge of such factors, analogous to installing new gauges in the laboratory, would offer more precise constraints for modeling. Such constraints on temperature, its spatial variation, and temporal evolution, would be especially valuable for studies concerned with the constitutive behavior of deformation under midcrustal conditions [*Bürgmann and Pollard*, 1992, 1994; *Nevitt*, 2015], where many of these plutons were emplaced [e.g., *Riklin*, 1983; *Ague and Brimhall*, 1988].

In this contribution, we synthesize previous investigations of the development of dikes, joints, faults, and ductile fabrics within the Lake Edison granodiorite of the Mount Abbot Quadrangle and the conditions under which these structures formed. We collected samples throughout the pluton representative of the penetrative "regional" fabric and locally strong "fault-related" fabrics for microstructural analysis and titanium-in-quartz (TitaniQ) thermobarometry. Uncertainties in TiO_2 activity and calibration choice, in addition to incomplete Ti reequilibration in the fault-related fabrics, restricted the usefulness of TitaniQ for calculating quantitative temperature estimates. We interpret the microstructural temperature estimates in the context of a 1-D heat conduction model to place constraints on the timing of jointing, faulting, and fabric development. The results allow us to integrate these various structures into a regional framework, which highlights the potential significance of kilometer-scale kink bands in influencing the spatial distribution of dominantly brittle and ductile structures in cooling plutons, particularly in transpressive settings.

2. Geologic and Tectonic Setting

2.1. Intrusive History

The Sierra Nevada Batholith was emplaced in a magmatic arc setting during subduction of the paleo-Pacific plates from 125 to 83 Ma [*Stern et al*., 1981]. While it remained the site of arc magmatism, the Sierra Nevada likely was characterized by a high geothermal gradient, similar to those observed in modern magmatic arcs, due to the movement of magma and the resulting heat transfer [*Dumitru*, 1990]. Modern arcs, such as the Cascade Range and the Andes, have geothermal gradients estimated to range from 25 to 30°C km^{-1} [*Morgan*, 1984] to 45°C km^{-1} [*Blackwell et al*., 1990]. At ~80 Ma, the angle of subduction under the Sierra Nevada shallowed, resulting in an eastward migration of the magmatic arc [*Burchfiel and Davis*, 1975; *Coney and Reynolds*, 1977; *Dickinson and Snyder*, 1978; *Dumitru*, 1990]. This transformed the Sierra Nevada region into a fore-arc basin setting [*Engebretson et al*., 1985], which significantly altered the thermal regime. Fore-arc settings typically have low geothermal gradients, due to underriding of the cold subducting plate [*Dumitru*, 1990; *Dumitru et al*., 1991]. By approximately 30–15 Ma, the geothermal gradient reached an extremely low value of ~5–15°C km^{-1} [*Dumitru*, 1990]. This significant change in thermal regime at 80 Ma coincided with deformation in the Mount Abbot Quadrangle at approximately 85–79 Ma [*Segall et al*., 1990].

The plutons located within the Mount Abbot Quadrangle are late Cretaceous in age and are members of the John Muir Intrusive Suite, which was emplaced during the last major pulse of Sierra Nevada magmatism [*Bateman*, 1992]. The NW-trending plutons are characterized by elongate geometries and crystallization ages that decrease toward the NE [*Lockwood and Lydon*, 1975; *Stern et al*., 1981]. The two plutons considered in this paper are the Lake Edison granodiorite ("Kle"; 88 ± 1 Ma) [*Tobisch et al*., 1995] and the younger Mono Creek granite ("Kmc"; 86 Ma) [*Tikoff and de Saint Blanquat*, 1997], which previously was referred to as the quartz monzonite of Mono Recesses [*Lockwood and Lydon*, 1975] (Figure 1).

The Lake Edison pluton, which is approximately 50 km-long, is narrow in the middle section and bulges laterally at both ends [*Bateman*, 1992]. The fine- to medium-grained granodiorite is composed of quartz, plagioclase (oligoclase), K-feldspar, biotite, hornblende, and sphene [*Pennacchioni and Zucchi*, 2013], and

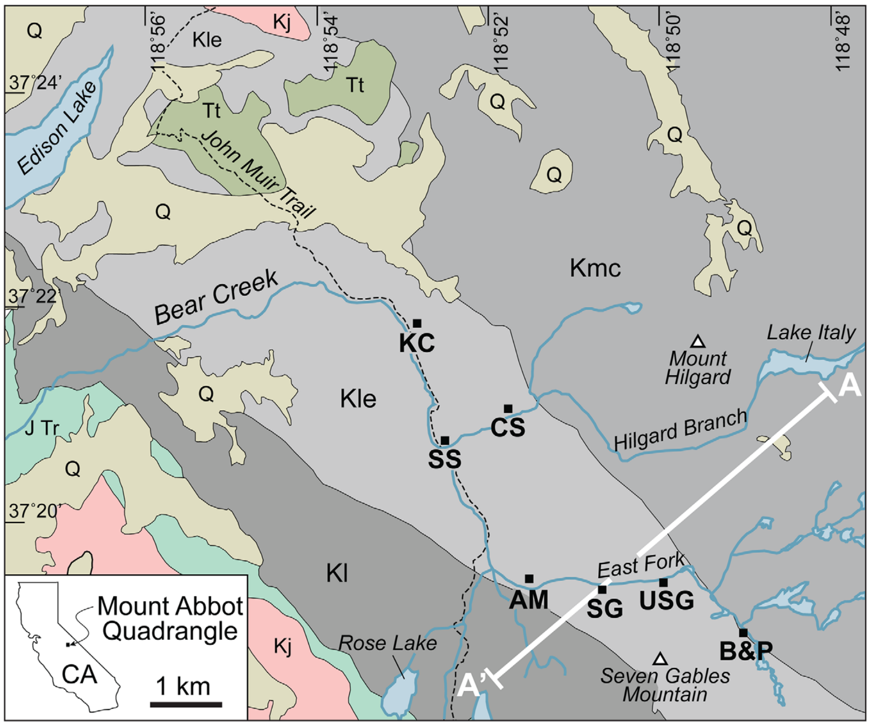

Figure 1. Geologic map of the Bear Creek field area in the southern portion of the Mount Abbot Quadrangle: Kmc, Mono Creek granite; Kle, Lake Edison granodiorite; Kl, Lamarck granodiorite; Kj, granitic rocks of uncertain affinities; J Tr, Metavolcanic rocks; Tt, olivine trachybasalt; Q, alluvium (modified from *Lockwood and Lydon* [1975]). The Mount Givens pluton is located ~5 km to the southwest of the Lamarck pluton. Outcrops sampled for this study include Kip Camp (KC), Sheared Schlieren (SS), Contractional Step (CS), Ape Man (AM), Seven Gables (SG), and Upper Seven Gables (USG). Also shown is the sample location (B&P) from *Bestmann and Pennacchioni* [2015]. The reader is referred to the .kmz file in the supporting information for a more detailed map (that includes the location of the Mount Givens pluton) and photos of the sampled outcrops.

exhibits a vertical or steeply dipping foliation approximately parallel to the pluton boundaries. The foliation is weakly developed and is defined by the alignment of mafic minerals and flattened xenoliths. The Lake Edison pluton intrudes the Lamarck and Mount Givens granodiorites to the southwest, and is intruded by the Mono Creek granite in the northeast. The Mono Creek granite has blocky alkali feldspar megacrysts within a medium-grained matrix containing biotite, minor hornblende, and sphene [*Lockwood and Lydon*, 1975; *Bateman*, 1992].

2.2. Deformation History

2.2.1. Rosy Finch Shear Zone

The oldest structure in the field area is the right-lateral Rosy Finch Shear Zone (RFSZ; Figure 2), an 80 km-long section of the 300 km-long Sierra Crest Shear Zone, which spans the axis of the Sierra Nevada magmatic arc [*Tikoff and Teyssier*, 1992; *Tikoff*, 1994; *Green and Schweickert*, 1995]. The Rosy Finch Shear Zone, believed to have played an important role in accommodating intruding plutons within this transpressional setting, is defined by a width that varies from 1 to 4 km and is greatest in the central part of the Mono Creek granite [*Tikoff and Teyssier*, 1992]. It is characterized by an *S-C* foliation, with both *S*- and *C*-planes oriented subvertically, and with a subhorizontal lineation. Based on kinematic relations and microstructural evidence, the Rosy Finch Shear Zone is interpreted to have initiated in unsolidified magma during pluton emplacement [*Tikoff and Teyssier*, 1992]. The shear zone remained active following pluton crystallization, as evidenced by medium- to low-temperature solid state microstructures that overprint the magmatic fabric within the center of the shear zone [*Tikoff and Teyssier*, 1992; *Tikoff and de Saint Blanquat*, 1997; *Titus et al.*, 2005]. Bulk fabrics within granitic plutons reflect the pluton cooling history and the temperature of the country rock during emplacement and deformation [*Schofield and D'Lemos*, 1998]. The progression of synmagmatic to high-, medium-, and low-temperature solid state microstructures in the Mono Creek pluton indicate that the host rock temperature decreased during deformation.

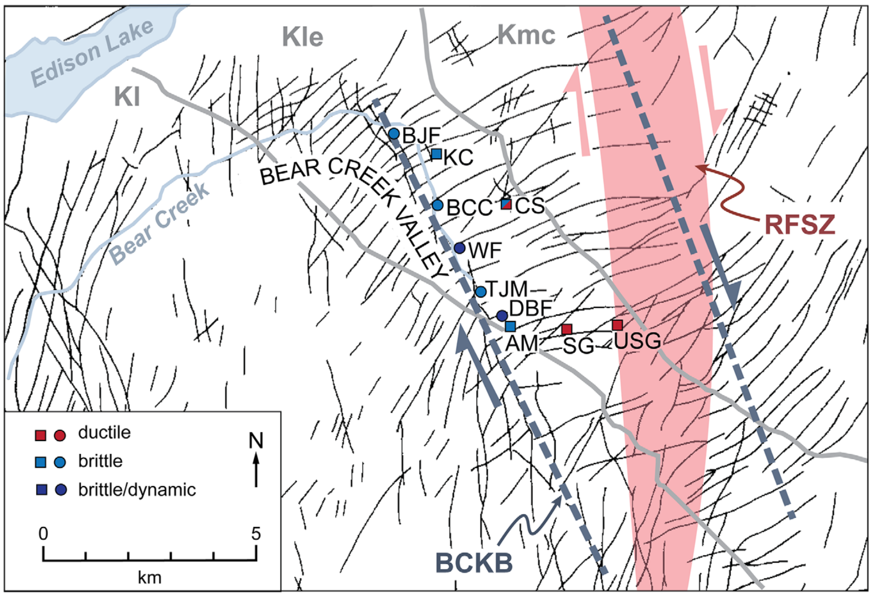

Figure 2. Outcrops investigated in the Mount Abbot Quadrangle, mapped with the outline of the Lake Edison pluton from Figure 1, the Bear Creek Kink Band (BCKB, delineated by the dashed dark blue lines), and the Rosy Finch Shear Zone (RFSZ, pink region). Squares indicate outcrops used for TitaniQ and microstructural analyses in this study; circles indicate outcrops presented in previous studies: BJF, Big Juniper Fault [*Griffith et al*., 2009a, 2009b]; BCC, Bear Creek Camp [*Martel et al*., 1988]; WF, Waterfall [*Martel*, 1990]; TJM, Trail Junction Meadows [*Martel et al*., 1988]; and DBF, Dancing Burn Fault [*Kirkpatrick et al*., 2009]. Outcrops near "CS" contain prominent brittle and ductile features; thus, it is labeled as both "brittle" and "ductile." The base map shows the traces of the major lineaments in the southern half of the Mount Abbot Quadrangle [*Davies and Pollard*, 1986; modified from *Lockwood and Lydon*, 1975]. The placement of the RFSZ is taken from *Tikoff and de Saint Blanquat* [1997].

Deformation within the Rosy Finch Shear Zone is hypothesized to have initiated during or immediately following emplacement of the Lake Edison granodiorite at 88 $\pm$ 1 Ma [*Tikoff and Teyssier*, 1992; *Tobisch et al*., 1995] and likely continued through the closure temperature for biotite at 80 Ma [*Tikoff and de Saint Blanquat*, 1997] (Figure 3). Models of porphyroclast rotation suggest that the Rosy Finch Shear Zone produced 1.2–8 km of right-lateral offset, though an unspecified amount of that offset occurred in a magmatic state [*Tikoff and Teyssier*, 1994; *Pachell et al*., 2003].

2.2.2. Dikes

Significant attention has been given to a variety of meter-scale structures–including dikes, joints, faults, and fault zones–throughout the Mount Abbot Quadrangle. The Lake Edison and Mono Creek plutons both are intruded by late-stage aplite and pegmatite dikes that range in thickness from $<$10 to 200 cm and can be up to several hundred meters in length [*Evernden and Kistler*, 1970; *Christiansen and Pollard*, 1997; *Pachell and Evans*, 2002]. *Christiansen and Pollard* [1997] characterized two generations of dikes. The older set includes pegmatite and aplite dikes oriented nearly parallel to the contact between the Mono Creek and Lake Edison plutons (140–180°), while the younger set is composed primarily of aplite with more variable orientations, ranging from 0-130°. Within the younger set, subvertical dikes that strike 090°$\pm$20° served as nucleation sites for left-lateral mylonitic shear zones. These mylonitic shear zones vary in width from 1 to 15 cm, are up to $\sim$300 m in length, and have offsets ranging from $<$1 to $\sim$10 m. Sheared dikes both widened and propagated in-plane as they accumulated offset, which led to linkage of shear zone segments and overall shear zone growth [*Christiansen*, 1995; *Christiansen and Pollard*, 1997].

2.2.3. Joints and Faults

The sheared dikes are crosscut by mineralized joints and faults [*Christiansen*, 1995]. Within the Bear Creek drainage, these fractures strike 050–070° and dip steeply to the south [*Segall and Pollard*, 1983b]. Joint development has been attributed to both thermal and tectonic stresses that accumulated during postmagmatic cooling [*Segall and Pollard*, 1983a; *Bergbauer*, 1998; *Bergbauer and Martel*, 1999]. Joints range in length from approximately one meter to tens of meters and commonly are composed of numerous echelon segments. The spacing between joints also is variable, ranging from centimeters to tens of meters [*Segall and Pollard*, 1983a].

Some joints were reactivated as left-lateral faults, as evidenced by the similar orientation, length-scale, and mineral fill for the joint and fault sets [*Segall and Pollard*, 1983b]. The faults offset dikes and xenoliths by several millimeters to several meters and have slickensides that plunge $<20°$ to the east, indicating approximately left-lateral strike slip [*Segall and Pollard*, 1983b; *Martel et al*., 1988; *Bürgmann and Pollard*, 1994; *Griffith et al*., 2008; *Nevitt et al*., 2014]. The faults did not propagate beyond the traces of the precursor joints as shear fractures, but some produced oblique wing cracks [*Segall and Pollard*, 1983b].

The joints and faults are filled with hydrothermal minerals, including epidote, chlorite, and quartz, indicating the fractures served as paleofluid conduits [*Segall and Pollard*, 1983a, 1983b; *Martel et al*., 1988]. In addition, alteration haloes occur adjacent to fractures where the host granodiorite has a bleached appearance [*Segall and Pollard*, 1983b; *Segall and Simpson*, 1986]. These alteration haloes are interpreted to have formed due to microcracking and fluid infiltration of the host granodiorite, which led to seriticization of feldspar [*Segall and Simpson*, 1986; *Ritz et al*., 2015]. *Kronenberg et al*. [1990] analyzed transmitted electron microscope images of deformed Lake Edison granodiorite and identified microcracks decorated with fluid inclusions. They concluded that the presence of fluids had a profound weakening effect on the granodiorite, particularly in areas of elevated pressure (i.e., within contractional fault steps).

2.2.4. Secondary Structures and Fault Growth

Fault slip caused stress perturbations and resulted in asymmetric secondary structures adjacent to fault tips [*Segall and Pollard*, 1980; Bürgmann and Pollard, 1994]. The most ubiquitous secondary structures are wing cracks, which occur in the NE and SW quadrants of fault tips and formed at angles ranging from 15–35° [*Martel and Pollard*, 1989] to 50° [*Bürgmann and Pollard*, 1992] counterclockwise to the fault planes. Wing cracks have apertures ranging up to $\sim$2 cm and are filled predominantly with quartz and, to a lesser extent, epidote. The NW and SE quadrants of fault tips commonly exhibit a locally strong mylonitic foliation [*Bürgmann and Pollard*, 1992, 1994].

Brittle (i.e., wing cracks) and ductile (i.e., mylonitic foliation) secondary structures are abundant within fault steps due to fault tip interaction [*Segall and Pollard*, 1980; Bürgmann and Pollard, 1992, 1994; *Nevitt and Pollard*, 2017]. Contractional steps are found at right-stepping discontinuities along the left-lateral faults, and contain a locally strong *S-C* mylonitic fabric that is restricted to the area between the step-bounding faults; immediately outside the step-bounding faults, the granodiorite is characterized by the weak regional fabric. Conversely, extensional steps are found at left-stepping discontinuities along left-lateral faults, and typically contain opening-mode fractures and veins that may accommodate up to $\sim$70% of the fault slip across the step [*Bürgmann and Pollard*, 1994].

In many cases, wing cracks at fault tips or in fault steps led to end-to-end linkage of echelon fault arrays. In addition, abundant oblique fractures between closely spaced noncoplanar faults facilitated side-to-side linkage and the development of simple fault zones that produce up to 10 m of slip [*Martel et al*., 1988; *Martel and Pollard*, 1989]. Fault zone slip primarily occurs along the boundary faults, which develop a cataclastic texture overprinting a mylonitic foliation [*Martel et al*., 1988]. Compound fault zones, which are up to several kilometers in length and accrue up to 100 m of slip, developed as oblique wing cracks linked simple fault zones to produce noncoplanar faults [*Martel*, 1990].

2.2.5. Proposed Relationships Between Meter-Scale and Kilometer-Scale Structures

Deformation and erosion within fault zones results in soil- and vegetation-filled troughs, which can be identified as lineaments on aerial photographs (mapped in Figure 2) [*Lockwood and Lydon*, 1975]. Within the Mount Abbot Quadrangle, the lineaments undergo a clockwise rotation to form a right-lateral monoclinal kink band, which is 4.8 km wide and $\sim$15 km long [*Davies and Pollard*, 1986; *Pachell et al*., 2003]. Kink bands also occur at the outcrop-scale in the Lake Edison granodiorite [*Segall and Pollard*, 1983b; *Davies and Pollard*, 1986]. While geometrically similar to kink bands found in laminated or foliated rocks [e.g., *Ramsay*, 1967], the slipping surfaces in the granodiorite are closely spaced left-lateral faults [*Segall and Pollard*, 1983b; *Davies and Pollard*, 1986]. The kilometer-scale Bear Creek Kink Band (BCKB, Figure 2) is interpreted to have formed during the last stage of right-lateral transpression that initiated with the Rosy Finch Shear Zone development [*Pachell et al*., 2003]. The apparently conjugate relationship between the Bear Creek Kink Band and left-lateral faults led *Davies and Pollard* [1986] to conclude that the kink band and faults developed coevally. Using kinematic relationships, *Pachell et al*. [2003] determined that the geometry of the Bear Creek Kink Band represents $\sim$3.7 km of right-lateral offset with as much as 148 m of slip along the left-lateral faults.

Alternatively, *Tikoff et al*. [1998] argued that the left-lateral faults and shear zones are related to the Rosy Finch Shear Zone in a conjugate sense. In this interpretation, the left-lateral faults correspond to the R' orientation relative to the shear zone for a Riedel-type fracture system [*Tikoff*, 1994; *Tikoff et al*., 1998]. However, the discrepancy between the strain magnitude of the Rosy Finch Shear Zone (up to 0.1) [*Tikoff and Teyssier*, 1994] and the left-lateral shear zones (up to 100) [*Christiansen and Pollard*, 1997] indicates that a conjugate relationship between the two types of structures is unlikely [*Christiansen and Pollard*, 1998]. In addition, the theory of Riedel-type fracture systems assumes intact rock, which was not the case for the Mount Abbot Quadrangle following nucleation of the joint set.

2.2.6. Timing of Deformation

Jointing and faulting likely occurred between 85 and 79 Ma (Figure 3), based on K-Ar and $^{40}Ar/^{39}Ar$ dating of white mica (muscovite and sericite) in the altered host granodiorite adjacent to faults [*Segall et al*., 1990; *Pachell and Evans*, 2002]. White mica is interpreted to have grown following fault slip and hydrothermal circulation within the microfractured granodiorite. The K-Ar and $^{40}Ar/^{39}Ar$ dating techniques yielded average ages of 78.9 $\pm$ 0.4 Ma [*Segall et al*., 1990] and 79.7 $\pm$ 0.16 Ma [*Pachell and Evans*, 2002], which represents the minimum age of faulting. Based on the greenschist facies mineral assemblage infilling joints in the Mount Givens granodiorite at Lake Florence [*Segall and Pollard*, 1983a], *Segall et al*. [1990] concluded that the maximum age of jointing likely corresponds to the cooling age of hornblende (85 Ma) in the Lake Edison granodiorite. However, *Pennacchioni and Zucchi* [2013] conclude that the joints must have formed at $>$500°C, making 85 Ma a minimum age estimate since the closure temperature for hornblende is 530 $\pm$ 45°C [*Harrison*, 1981].

2.2.7. Temperature Evolution and Spatial Variation During Deformation

The microstructure and composition of minerals infilling the faults reveal several episodes of slip and fluid infiltration under evolving ambient conditions [*Griffith et al*., 2008]. While the fracture-filling minerals appear undeformed in the joints, they are strongly mylonitized and cataclasized in the faults [*Segall and Pollard*, 1983b; *Griffith et al*., 2008]. The small left-lateral faults primarily consist of quartz mylonite, in which the quartz has been recrystallized to a fine grain size (10–100 μm) and has a shape-preferred orientation consistent with left-lateral shear [*Griffith et al*., 2008]. Furthermore, the recrystallized quartz is characterized by a strong crystallographic preferred orientation, in which the c-axes form an oblique single girdle, again consistent with left-lateral shear [*Griffith et al*., 2008]. This mylonitic fabric often is overprinted by cataclasite, which generally is associated with epidote-rich veins and sometimes with zeolite veins [*Martel et al*., 1988; *Griffith et al*., 2008]. In rare cases, pseudotachylyte also is found within the faults [*Griffith et al*., 2008; *Kirkpatrick and Shipton*, 2009; *Kirkpatrick et al*., 2009]. *Griffith et al*. [2008] conclude that this sequence preserves a record of aseismic ductile shearing, brittle shearing, seismic slip, and further cooling and opening. This sequence suggests a temperature decrease over the lifespan of the faults.

In addition, *Bürgmann and Pollard* [1994] observed spatial variation in the prevalence of brittle and ductile deformation features across the Lake Edison pluton, with outcrops closest to the contact with the Mono Creek pluton exhibiting stronger foliations and fewer splay fractures associated with faulting (Figure 2). Based on this observation and numerical modeling, they hypothesized that intrusion of the Mono Creek pluton resulted in a temperature gradient across the Lake Edison granodiorite during faulting. In addition, *Pennacchioni and Zucchi* [2013] document greater fault slip and off-fault ductile deformation near the pluton contact, suggesting that high-temperatures were longer-lived there. Our analysis of TitaniQ and heat conduction modeling provide a direct test of this temperature gradient hypothesis, which we further address in the Discussion section.

2.2.8. Estimating the Lithostatic Pressure During Deformation

Previous studies have quoted a broad range of lithostatic pressure, from 100 to 400 MPa, for deformation in the Mount Abbot Quadrangle [*Ague and Brimhall*, 1988; *Martel et al*., 1988; *Bergbauer and Martel*, 1999; *Griffith et al*., 2008; *Nevitt et al*., 2014]. Amphibole geobarometry used throughout the Sierra Nevada provides constraints for the pressure during pluton emplacement [*Ague and Brimhall*, 1988; *Brady et al*., 2006; *Nadin*, 2007; *Nadin and Saleeby*, 2008; *Chapman et al*., 2012]. Such analyses measure emplacement pressures at the elevation of the current erosional level, which ranges from $\sim$450 to 3300 m in the sampled regions. Emplacement pressure in the central Sierra Nevada ranges from $\sim$200 to 400 MPa and generally decreases from west to east. Contoured maps of emplacement pressure (included as an overlay in the .kmz file in the supporting information and based on *Nadin* [2007] and *Nadin and Saleeby* [2008]) illustrate that, with the exception of the southern-most portion of the Sierra Nevada, contour lines of equal

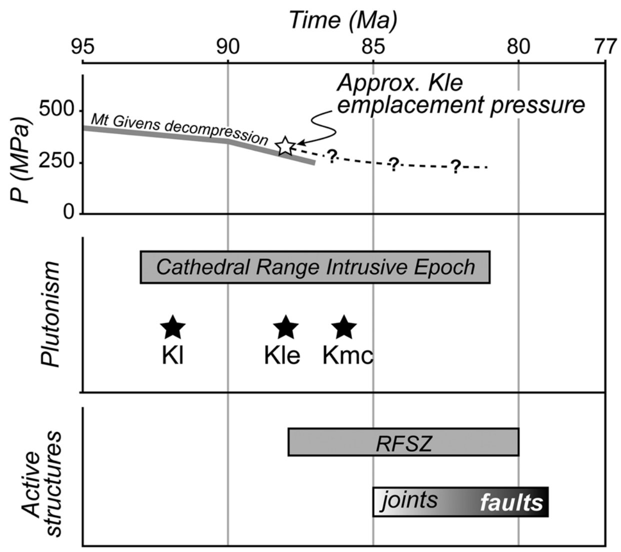

Figure 3. Lithostatic pressure (P) during deformation in the Mount Abbot Quadrangle. Geobarometry data shows the decompression path for the nearby Mount Givens granitic pluton [*Renne et al.*, 1993], and the approximate emplacement pressure for Kle based on data from *Ague and Brimhall* [1988] and *Nadin* [2007]. Decompression occurred during the Cathedral Range Intrusive Epoch [*Evernden and Kistler*, 1970]. U-Pb zircon ages for the Lamarck (Kl), Lake Edison (Kle), and Mono Creek (Kmc) plutons are denoted by black stars. The timing of the Rosy Finch Shear Zone (RFSZ) [*Tikoff and Teyssier*, 1992] and the Bear Creek joints and faults [*Pachell and Evans*, 2002; *Segall et al.*, 1990] are indicated.

emplacement pressure approximately follow the NW-SE trend of the batholith. Therefore, to estimate the emplacement pressure for the Lake Edison pluton, we averaged the pressure at two sites closest to the pluton and aligned with its NW-SE trend (samples 348 and 117 from *Nadin* [2007]). The resulting estimate for the emplacement pressure of the Lake Edison granodiorite is 315 MPa at the current erosional level (Figure 3).

During and following emplacement of the Lake Edison granodiorite at 88 ± 1 Ma [*Tobisch et al.*, 1995], the central Sierra Nevada underwent significant decompression due to exhumation and/or uplift [*Renne et al.*, 1993]. Based on amphibole geobarometry data from the Mount Givens pluton located in the Mount Abbot Quadrangle south of the field area in Figure 1 (see .kmz file in supporting information) [*Lockwood and Lydon*, 1975], the region experienced decompression of $\sim$100 MPa between 90 and 87 Ma [*Renne et al.*, 1993]. Furthermore, petrologic evidence suggests that the Cathedral Range Intrusive Epoch (93–81 Ma) was accompanied by enhanced pluton unroofing and related decompression [*Mansfield*, 1979]. Assuming that the Lake Edison granodiorite followed the decompression path of the Mount Givens pluton, the maximum pressure during jointing and faulting in the Lake Edison granodiorite would be $\sim$280 MPa (Figure 3). It is likely, however, that the region continued to decompress by an uncertain amount during the remainder of the Cathedral Range Intrusive Epoch. We suggest that 250 MPa is a reasonable estimate for the lithostatic pressure during faulting in the Mount Abbot Quadrangle, as illustrated in Figure 3.

3. New Temperature Constraints: Methods and Results

We analyzed a total of 12 samples from 6 outcrops in the Lake Edison granodiorite at varying distances from the contact with the Mono Creek granite. For each outcrop, we selected one sample characteristic of the regional foliation (collected away from faults and exhibiting only weak regional foliation to the naked eye) and one sample characteristic of the fault-related deformation (collected within a ductilely deformed contractional fault step, or in a ductilely deformed region directly adjacent to fault tip). Photos of each outcrop are included as links in the .kmz file in the supporting information. The following sections detail microstructural and TitaniQ analyses for these samples and compare the results to a thermal conduction model of the Lake Edison pluton following intrusion of the Mono Creek pluton.

3.1. Microstructural Observations

Regional (Figure 4) and fault-related (Figure 5) samples are characterized by distinct microstructural features indicative of higher and lower temperatures (or lower and higher strain rates) of deformation, respectively. Regional samples typically contain medium-grained (150–200 μm) quartz with interlobate grain boundaries, characteristic of grain boundary migration (GBM), and weak subgrain development, suggestive of subgrain rotation (SGR) recrystallization (Figure 4a). GBM and SGR recystallization mechanisms are estimated to both be active in quartz at 400–500°C [*Lloyd and Freeman*, 1994; *Stipp et al.*, 2002; *Passchier and Trouw*, 2006]. Transitions between quartz recrystallization mechanisms, however, are highly sensitive to strain rate and

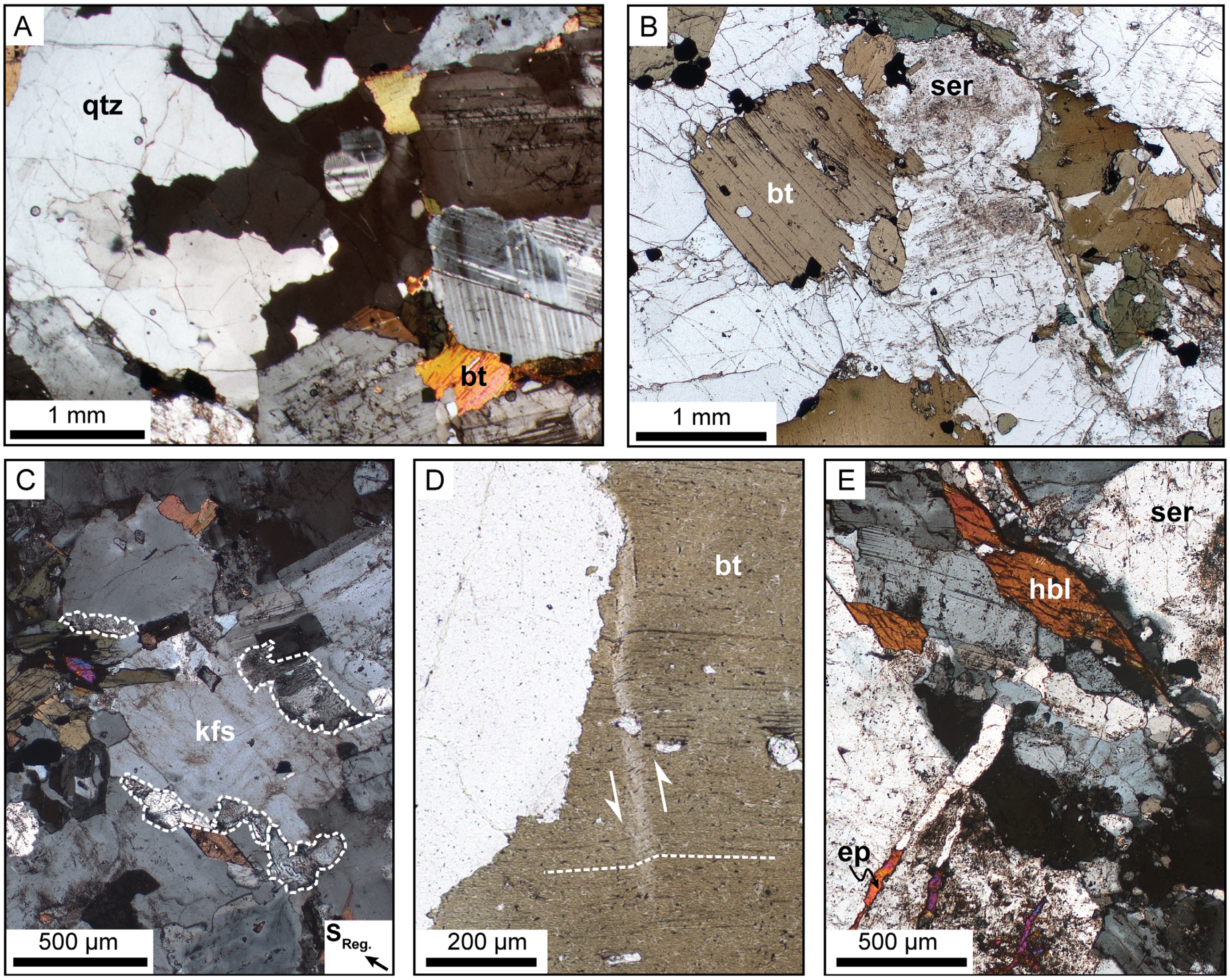

Figure 4. Regional foliation: (a) quartz with interlobate grain boundaries characteristic of GBM recrystallization and polygonal feldspar grains (sample TC11-05); (b) Blocky biotite, aggregates of biotite and hornblende, and sericitized feldspar (sample SS12-03); (c) myrmekite, outlined by dashed white line, oriented along grain boundaries parallel to S_{Reg} (sample AM11-01); (d) left-lateral kink band within biotite grain (sample SG10-08); (e) fractured hornblende grain and microfracture infilled with quartz and epidote, surrounded by sericite.

fluid composition [e.g., *Hirth and Tullis*, 1992; *Chernak et al.*, 2009; *Kidder et al.*, 2016], which limits their reliability as temperature indicators.

Feldspar grains (<3 mm), while roughly polygonal in regional samples, typically contain irregular boundaries, suggesting the onset of plastic deformation mechanisms. Additional indicators of plastic deformation in feldspar include bent twinning in plagioclase, flame perthite development in K-feldspar, and the widespread occurrence of myrmekite (Figure 4c). Myrmekite occurs preferentially on surfaces parallel to the trend of the regional foliation and perpendicular to the inferred orientation of the most compressive principal stress [*Simpson and Wintsch*, 1989]. As viewed in the XZ plane, biotite grains range in shape from euhedral to splinter-like, with grain sizes ranging from 0.5 to 5 mm, respectively (Figure 4b). Some biotite grains have tails that taper in the direction of the regional foliation and biotite rarely occurs in the pressure shadows of feldspar porphyroclasts. In addition, biotite rarely contains kink bands (Figure 4d). Elongate aggregates of biotite, hornblende (< 3 mm), and sphene (<1 mm) are common and help define the NW-trending regional foliation. Feldspar, hornblende, and sphene grains often contain microfractures filled primarily with quartz and occasionally with epidote ± chlorite (Figure 4e). Biotite alteration to chlorite and feldspar

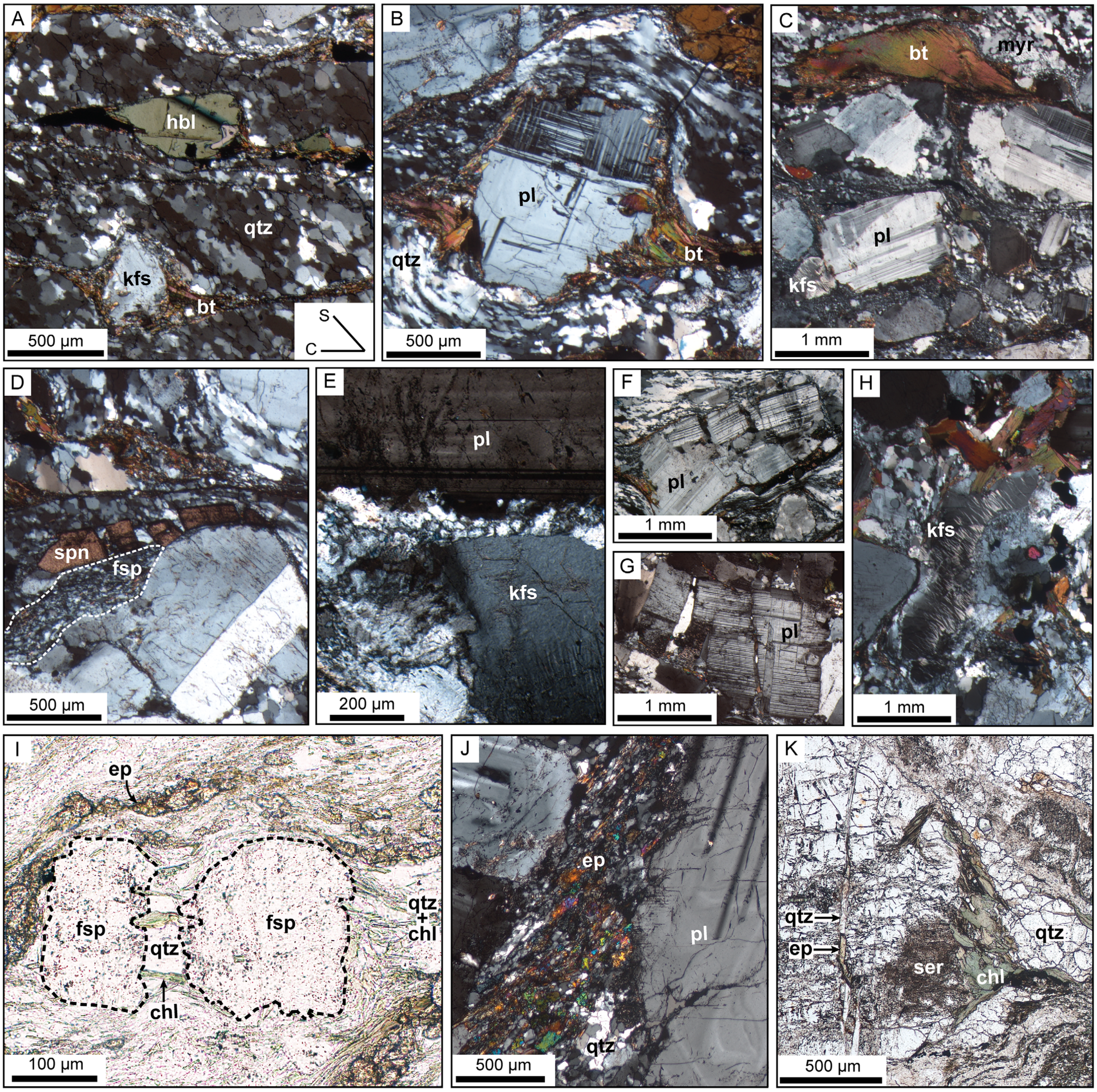

Figure 5. Fault-related foliation: (a) *S-C* fabric with hornblende fish and biotite growing in pressure shadow of K-feldspar porphyroclast (sample CS12-03); (b) biotite growth in pressure shadows of plagioclase porphyroclast (sample IS12-02; (c) biotite fish (sample SG10-03); (d) fragmented sphene and fine-grained feldspar (fsp) (sample CS12-03); (e) bulging texture between two feldspar grains (sample SG10-04); (f and g) fractured plagioclase (samples AM11-02 and SG10-02, respectively); (h) flame perthite in K-feldspar (sample IS12-01); (i) chlorite and quartz growth within feldspar pull-apart and pressure shadow with abundant epidote surrounding (sample SG10-12); (j) epidote growth in pressure shadow of plagioclase grain (sample USG12-11); and (k) quartz and epidote present in microfracture, chlorite after biotite in pressure shadow and abundant sericite (sample USG12-01).

alteration to sericite is commonly observed, even at significant distances (~10 m) from the nearest fracture visible at the outcrop (Figure 4).

In contrast to the weak regional fabric, fault-related samples are characterized by a strong *S-C* mylonitic foliation [*Lister and Snoke*, 1984] with a left-lateral sense of shear. The *C*-plane is defined by the alignment of biotite grains and very fine-grained feldspar, while the *S*-plane is defined by a shape-preferred orientation

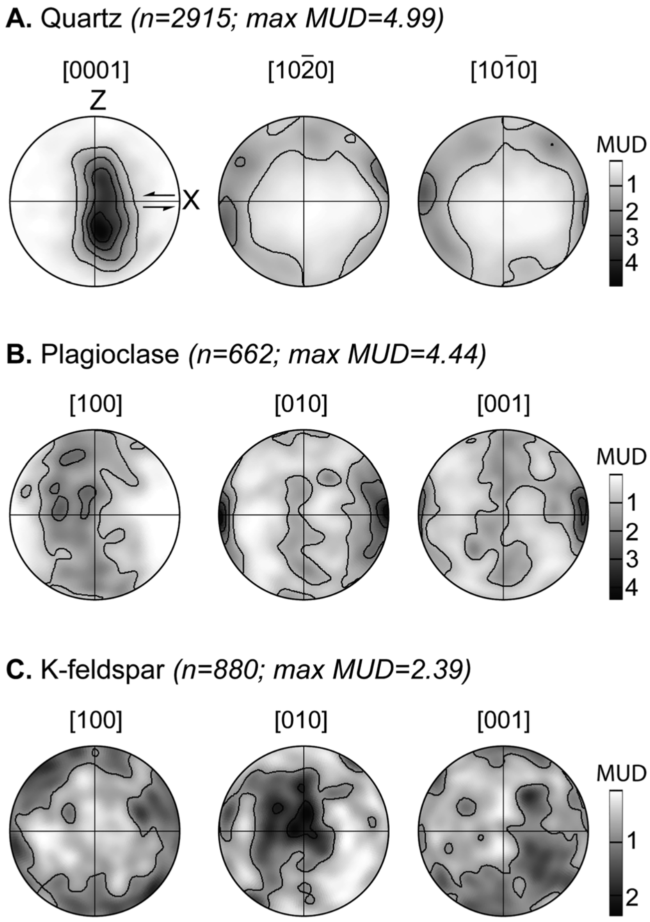

Figure 6. Lower hemisphere, equal area pole figures for (a) quartz, (b) fine-grained plagioclase, and (c) fine-grained K-feldspar. Pole figures are plotted as one point per grain and the number of grains is indicated by *n*. Contouring was calculated using a 15° half-width and as multiples of uniform density (MUD), with maximum MUD value indicated.

in quartz (Figure 5a). Subgrains and recrystallized grains in quartz have similar sizes, suggesting recrystallization was dominated by progressive SGR. Biotite, which often forms in the pressure shadows of feldspar porphyroclasts (Figure 5b) and as mica fish (Figure 5c), appears to have been stable during deformation, indicating a temperature greater than 250°C [*Stesky et al*., 1974; *Stesky*, 1978; *Passchier and Trouw*, 2006]. Hornblende fish also are observed (Figure 5a), in addition to fractured and fragmented hornblende and sphene grains (Figure 5d). Hornblende remains brittle up to temperatures of 650–700°C, which provides an upper bound on the temperature of deformation [*Nyman et al*., 1992; *Babaie and La Tour*, 1994; *Berger and Stünitz*, 1996; *Passchier and Trouw*, 2006].

The fine-grained plagioclase found along the *C*-plane and surrounding feldspar porphyroclasts (Figures 5d and 5e) has been interpreted to represent either cataclastic flow [*Bürgmann and Pollard*, 1994] or recrystallization [*Pennacchioni and Zucchi*, 2013]. Deformed feldspar grains commonly contain microfractures (Figures 5f and 5g), consistent with brittle behavior. However, plagioclase and K-feldspar grains also exhibit bent twinning, flame perthite (Figure 5h), and bulging textures along grain boundaries (Figure 5e), suggesting the onset of plasticity. These feldspar microstructures suggest semibrittle behavior and are consistent with a temperature of 400–500°C [*Pryer*, 1993; *Pryer and Robin*, 1995; *Shigematsu*, 1999; *Passchier and Trouw*, 2006].

We interpret that myrmekite in fault-related samples likely preceded faulting, contrary to the conclusions of some previous studies [*Griffith et al*., 2008; *Pennacchioni and Zucchi*, 2013]. Myrmekite is pervasive in samples of the regional foliation (Figure 4c), where its orientation is consistent with the inferred remote principal stresses. Within mylonitized fault steps, however, myrmekite does not show a systematic occurrence in regions of inferred high pressure during fault slip [*Simpson and Wintsch*, 1989]. Moreover, *Bürgmann and Pollard* [1994] observed microfractures overprinting myrmekite within fault steps. Thus, we do not consider myrmekite development to be representative of fault-related deformation, but a preexisting microstructure inherited from the regional foliation.

Crystallographic preferred orientations (CPOs) for quartz and feldspar in fault-related samples were collected using electron backscatter diffraction (EBSD) analysis. Methodology for EBSD data collection and postprocessing used in this study is included in the supporting information. The c-axis pole figure for quartz (Figure 6a) indicates a strong CPO with a Y-maximum, suggesting that recrystallization was primarily accommodated by prism-<a> slip. The prism-<a> slip system in quartz is estimated to be active between temperatures of 400–600°C [*Schmid and Casey*, 1986; *Passchier and Trouw*, 2006]. The plagioclase pole figure (Figure 6b) also indicates a strong CPO with maxima in the [010] and [001] pole figures aligned with the shear plane. Although this is an atypical CPO for plagioclase [e.g., *Hansen et al*., 2013], it does indicate deformation by crystal plastic mechanisms. The K-feldspar pole figure (Figure 6c) shows a weak CPO, suggesting that crystal plasticity likely was not the primary deformation mechanism for K-feldspar.

Overprinting textures indicate that deformation may have continued at temperatures below 350°C. This includes the presence of epidote and chlorite within pressure shadows and feldspar pull-aparts (Figures 5i–5k), suggesting these lower-greenschist minerals were stable during late-stage deformation. Microcracks containing epidote, chlorite, and zeolite, also attest to at least minor deformation during lower greenschist conditions. In addition to the presence of these minerals, kinked and broken biotite grains commonly occur, suggesting late-stage deformation may have persisted at temperatures below the onset of plasticity in biotite (~250°C). Heavy seritization of feldspars is observed both in the fault-related samples (Figure 5k) and in regional samples collected meters away from joints and faults. Such alteration suggests that fluids continued to interact with and alter the granodiorite at temperatures below 350°C.

3.2. Titanium-In-Quartz (TitaniQ) Analysis

Titanium-in-quartz thermobarometry (referred to as TitaniQ) [*Huang and Audétat*, 2012; *Thomas et al.*, 2010; *Wark and Watson*, 2006] is a technique used to constrain the temperature and pressure of quartz deformation, based on the substitution of Ti for Si in quartz when a Ti-bearing phase (e.g., sphene) is present. The thermometer was first calibrated by *Wark and Watson* [2006], who measured titanium concentrations in synthetic quartz produced experimentally at 600–1000°C and at 1 GPa in the presence of rutile and aqueous fluids. *Thomas et al.* [2010] conducted additional experiments to establish the sensitivity of TitaniQ to changes in pressure. The *Thomas et al.* [2010] calibration is given by the following expression:

$$\mathrm{RT}\ \ln X_{\mathrm{TiO_2}}^{\mathrm{quartz}} = -60952 + 1.520\times \mathrm{T} - 1741\times P + \mathrm{RT}\ \ln a_{\mathrm{TiO_2}}, \tag{1}$$

where R is the universal gas constant (8.3145 J/K), T is temperature in Kelvin, $X_{\mathrm{TiO_2}}^{\mathrm{quartz}}$ is the mole fraction of TiO_2 in quartz, P is the lithostatic pressure, and $a_{\mathrm{TiO_2}}$ is the activity of TiO_2 in the system.

The *Thomas et al.* [2010] calibration was challenged by *Huang and Audétat* [2012], whose independent experiments indicate a dependence on growth-rate for Ti substitution. The *Huang and Audétat* [2012] calibration is given by the following equation:

$$\log\left(\mathrm{Ti}/a_{\mathrm{TiO_2}}\right) = -0.27943\cdot 10^4/\mathrm{T} - 660.53\cdot\left(\mathrm{P}^{0.35}/\mathrm{T}\right) + 5.6259, \tag{2}$$

where the activity term, $a_{\mathrm{TiO_2}}$, is incorporated into the equation as indicated by *Hayden and Watson* [2007]. The calibration of *Huang and Audétat* [2012] is based on their slowest experiments and yields temperatures ≥100°C higher than predicted by the *Thomas et al.* [2010] calibration. However, *Thomas et al.* [2015] argue that the experiments of *Huang and Audétat* [2012] had widely varying Ti content at any given P-T condition, indicative of disequilibrium that biased their analysis. *Thomas et al.* [2015] conducted additional experiments that confirmed Ti equilibrium, and thus the accuracy, of the *Thomas et al.* [2010] TitaniQ calibration.

There remains uncertainty and disagreement in the TitaniQ community regarding the accuracy of these calibrations. Previous studies have shown that the *Thomas et al.* [2010] calibration underestimates the quartz recrystallization temperature in the case of contact metamorphism [*Morgan et al.*, 2014] and overestimates Ti solubility in granite and rhyolite crystallizing from a melt by a factor of two to five [*Huang and Audétat*, 2012]. However, *Ashley et al.* [2013] and *Kidder et al.* [2013] tested the two calibrations on recrystallized quartz in amphibolite facies metapelites, and greenschist facies veins and quartzite, respectively, and found the *Thomas et al.* [2010] calibration to be more accurate. In this contribution, we present temperatures calculated using both methods, but limit our interpretation to relative temperature differences based on Ti concentrations measured in the samples. We report temperatures assuming $a_{\mathrm{TiO_2}}=0.8$, as has been done for other studies in sphene-bearing granitoids [*Kohn and Northrup*, 2009; *Behr and Platt*, 2011; *Nadin et al.*, 2016], with the significant uncertainty in this choice described in the Discussion section.

Methods of sample preparation and TitaniQ data collection are described in the supporting information. A minimum of 11 measurements was made in each sample for a total of 200 measurements. Five measurements were considered outliers (more than three standard deviations from the sample mean) and were excluded from further data reduction. The results are summarized in Table 1.

Table 1. Titanium-In-Quartz Data

Outcrop	Distance From Kmc (km)	Elevation (km)	Foliation Type	n^a	Ti (ppm) Median	Mean	Mean Std. Dev.
CS	0.4	2.9	Regional	17	28.2	27.4	9.6
			Fault-related	28	11.6	11.3	2.9
USG	0.4	3.2	Regional	11	22.5	24.6	8.7
			Fault-related	15	12.3	11.7	1.4
KC	1.1	2.8	Regional	9	34.5	33.7	10.7
			Fault-related	13	16.4	15.8	1.6
SG	1.4	3.1	Regional	15	29.2	29.6	8.6
			Fault-related	28	8.8	9.1	0.7
SS	1.8	2.9	Regional	17	41.0	37.9	14.4
			Fault-related	14	6.6	6.1	0.8
AM	2.4	3.0	Regional	11	30.5	29.9	12.9
			Fault-related	16	17.9	18.0	0.7

[a]Outliers (>3 standard deviations) removed.

3.2.1. Subsetting [Ti] Data According to Microstructure

Ti concentrations in quartz are observed to reequilibrate during grain boundary migration recrystallization at elevated temperatures (>500°C), even over very short time scales [*Grujic et al*., 2011]. We interpret that Ti concentrations associated with the regional foliation also reequilibrated during substantial high-temperature dynamic recrystallization indicated by a strong CPO (max. MUD $=\sim 7$) and a general lack of remnant magmatic CL patterns [e.g., *Wiebe et al*., 2007]. This interpretation is supported by the observation that Ti concentrations are not a function of grain size (Figure 7). The lack of correlation is consistent with a progressive reequilibration of Ti that keeps pace with temperature changes [e.g., *Cross et al*., 2015], and contrasts with a greenschist facies example from the Hsuehshan range, Taiwan, where convergence in Ti concentrations with decreasing grain size indicates only partial equilibration during recrystallization and cooling [*Kidder et al*., 2013]. Resetting of Ti concentrations during the formation of the regional foliation in the Lake Edison granodiorite also is supported by lower Ti concentrations (average $= 31 \pm 12$ ppm; Table 1) than undeformed granodiorites (49–105 ppm) in other field areas [*Johnson*, 2009; *Breiter et al*., 2013], further addressed in the Discussion. Because we interpret that Ti equilibrated in quartz, the deformation temperature is estimated using the average of all TitaniQ measurements made in each sample.

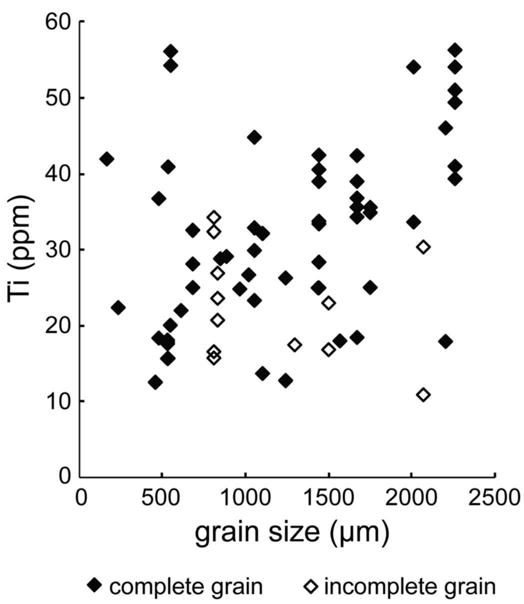

Figure 7. Ti content versus grain size for regional foliation samples. Grain size estimates are based on the longest observable diameter in two-dimensional petrographic analysis. Filled diamonds indicate that the entire grain boundary was observed, while open diamonds indicate measurements made on partial grains (those truncated by the thin-section boundary), thus representing minimum estimates for grain size.

In contrast to the regional foliation, fault-related samples show a distinct relationship between microstructure and Ti content, indicating that Ti equilibration did not occur homogeneously throughout the recrystallized zones. In fault-related samples, cathodoluminescence (CL) intensity correlates closely with Ti content (Figure 8), with dark and bright CL regions corresponding to low and high Ti concentrations, respectively. Figure 8b shows that regions of dark and bright CL occur in elongate bands running parallel to foliation. Quartz grains with dark CL and low Ti content often are located in the vicinity of biotite and other secondary phases (Figures 8c and 8d). We infer that Ti equilibration was enhanced within the dark CL bands, due to local exchange of Ti with secondary phases during deformation [*Nachlas and Hirth*, 2015]. In contrast, bright CL regions likely are

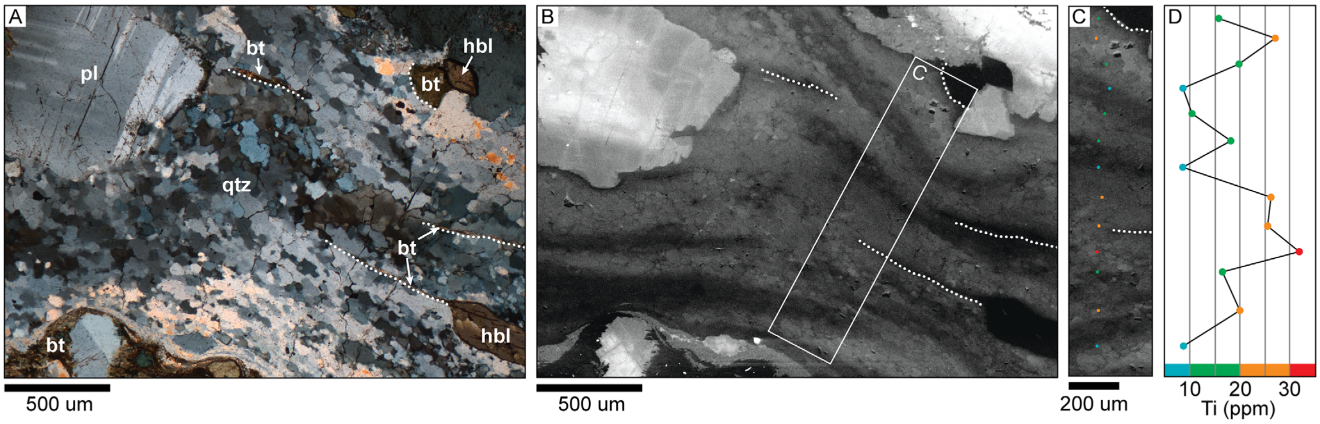

Figure 8. (a) Cross-polarized photomicrograph of fault-related fabric in sample SG10-03; (b) CL image of the same region of SG10-03; (c) Sites of SIMS analysis in this region; and (d) Graph of Ti concentration measured at each of the analysis sites in Figure 8c. CL intensity corresponds well with Ti content, thus the CL image in Figure 8B can be used as a proxy for Ti variation in this region. Quartz adjacent to secondary phases, notably biotite (white dotted lines), is characterized by lower CL intensity and inferred Ti content. Dark CL bands not adjacent to secondary phases in 6B may be the result of secondary phases in the third dimension.

characterized by Ti concentrations inherited from the regional foliation, which did not fully reequilibrate during deformation.

3.2.2. TitaniQ Results

Figure 9 and Table 1 summarize the TitaniQ data for each of the regional and fault-related samples. The data set average ± standard deviation for [Ti] in the regional foliation samples is 31 ± 12°C. For fault-related samples, only [Ti] measurements made within the dark CL regions (corresponding to the lowest 20% of data) were considered representative, resulting in a data set average ± standard deviation of 12 ± 4°C. For reference, the average of all measurements in fault-related samples is indicated by the dashed red line in Figure 9 with a data set average ± standard deviation of 21 ± 8°C.

In each outcrop, the fault-related foliation is characterized by lower Ti content than the corresponding regional foliation. Average temperatures calculated using the *Thomas et al*. [2010] calibration range from 486 to 519°C in the regional samples and from 396 to 464°C in the fault-related samples. Using the *Huang and Audétat* [2012] calibration, regional foliation samples have averages ranging from 618 to 660°C, while fault-related samples have averages ranging from 505 to 590°C. Given the uncertainty involved in the choice of calibration (further addressed in the Discussion), the most significant result of the TitaniQ analysis is the relative [Ti] difference of approximately 10–30 ppm between the regional and fault-related foliation samples (Figure 9). Moreover, we found no systematic trend between distance from the pluton contact and Ti content (Table 1 and Figure 9).

3.3. Thermal Models

Additional constraints on the deformation temperature are provided by the heat equation, which is used to model the evolving temperature gradient across the Lake Edison pluton following intrusion of the Mono Creek pluton. This provides a direct test of the hypothesis set forth by *Bürgmann and Pollard* [1994] that intrusion of the Mono Creek pluton produced a temperature gradient across the Lake Edison pluton at the time of faulting. Previous models of heat conduction associated with igneous intrusions have included both one and two-dimensional methods [*Norton and Knight*, 1977; *Harrison and Clarke*, 1979; *Barton and Hanson*, 1989; *Hanson and Barton*, 1989; *Peacock*, 1989; *Stowell and Pike*, 2000; *Nabelek et al*., 2012]. These models are based on the conservation of energy [*Mahon et al*., 1988]:

$$\frac{\partial Q}{\partial t}+\Phi+k\nabla^2 T=\rho c_p \frac{DT}{Dt}, \tag{3}$$

where $\partial Q/\partial t$ is the internal heat generation with time, Φ is the viscous dissipation function, k is the thermal conductivity, T is the temperature, ρ is the density, c_p is the specific heat capacity, and DT/Dt is the material time derivative of the temperature, given as

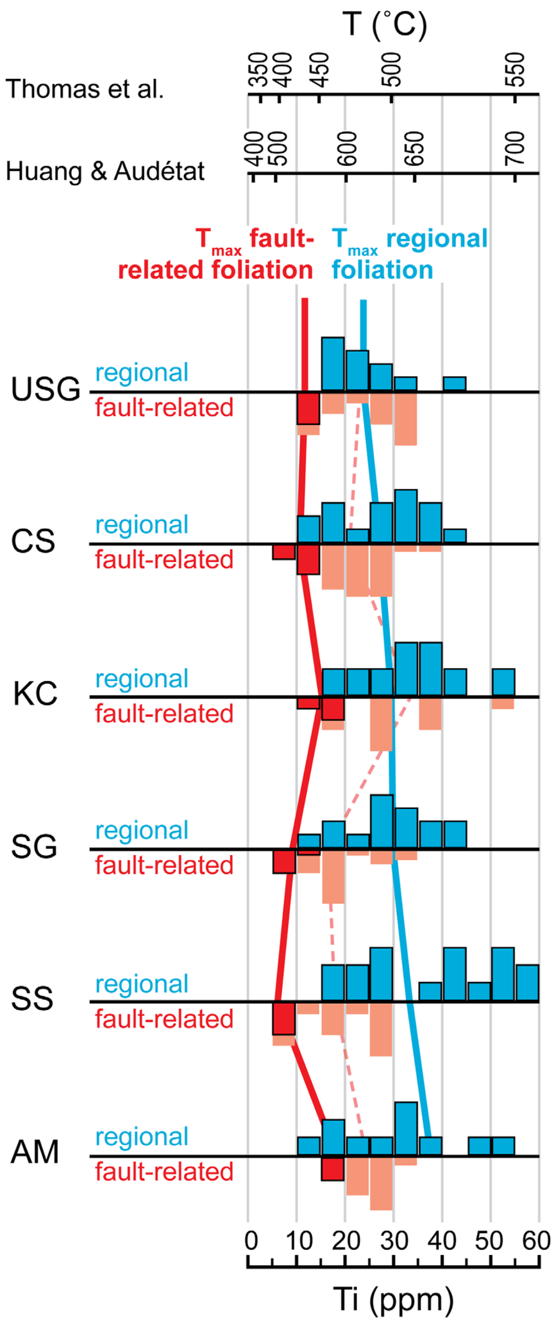

Figure 9. Ti concentrations measured in quartz and the corresponding temperatures calculated using the *Thomas et al.* [2010] and *Huang and Audétat* [2012] calibrations. For the regional samples, T_{max} is calculated as the bulk average. For the fault-related samples, T_{max} is the average of the measurements from the lowest 20% of data, which are interpreted to be the most re-equilibrated (shown as dark red). The dashed red line indicates the average of the total fault-related data set for each sample. Histograms are normalized by the maximum bin frequency for each sample.

$$\frac{DT}{Dt}=\frac{\partial T}{\partial t}+v\nabla T, \tag{4}$$

where v is the velocity. The term $v\nabla T$ represents thermal transport due to magma convection. It is common practice [e.g., *Barton and Hanson*, 1989; *Hanson and Barton*, 1989; *Nabelek et al.*, 2012; *Peacock*, 1989; *Stowell and Pike*, 2000] to neglect the thermal contributions of internal heat generation (e.g., latent heat of crystallization), viscous dissipation, and/or convection. By neglecting these terms, equation (3) reduces to the equation for conductive heat transfer:

$$\frac{\partial T}{\partial t}=\kappa\nabla^2 T, \tag{5}$$

in which κ is the thermal diffusivity and $\kappa=k/\rho c_p$. We use numerical and analytical solutions to the heat equation to produce models of heat conduction across the Lake Edison pluton in one and two-dimensions (Figures 10–12). Material properties used in all models are reported in Table 2.

3.3.1. Model Assumptions

The model requires a number of assumptions, including fast enough intrusion to avoid significant heat loss, uniform initial temperature throughout the host rock, and identical thermal properties for the host rock and intruding rock. The assumption of rapid intrusion is likely justified, since the rate of magma ascension is generally much faster than the rate of heat conduction through the crust [*Jaeger*, 1964; *Spera*, 1980; *Barton and Hanson*, 1989]. The plutons within the quadrangle all are of granitic affinities, thus thermal property contrasts between the plutons are not expected to significantly change the modeled temperature fields. *Delaney* [1987] shows that thermal property contrasts affect the maximum temperature reached in the host rock, but only over relatively short time periods (<1 Ma).

Another significant assumption is related to the geometry of the intruding pluton. The geometry of an elongate plutonic intrusion previously has been treated as an infinite slab of finite thickness, *2a* [e.g., *Harrison and Clarke*, 1979]. More commonly, this idealized geometry is used to characterize a dike intrusion [e.g., *Lovering*, 1935, 1936; *Pollard and Fletcher*, 2005]. *Lovering* [1935] provides the analytical solution to the heat equation for this specific geometry in one-dimension:

$$\theta=\frac{1}{2}\left[\operatorname{erf}\left(\frac{a+x}{2\sqrt{\kappa t}}\right)+\operatorname{erf}\left(\frac{a-x}{2\sqrt{\kappa t}}\right)\right], \tag{6}$$

in which erf is the error function, a is the half-width of the intrusion, x is distance from the center of the intrusion, κ is the thermal diffusivity, and t is time. θ is a nondimensional expression of temperature, defined as follows:

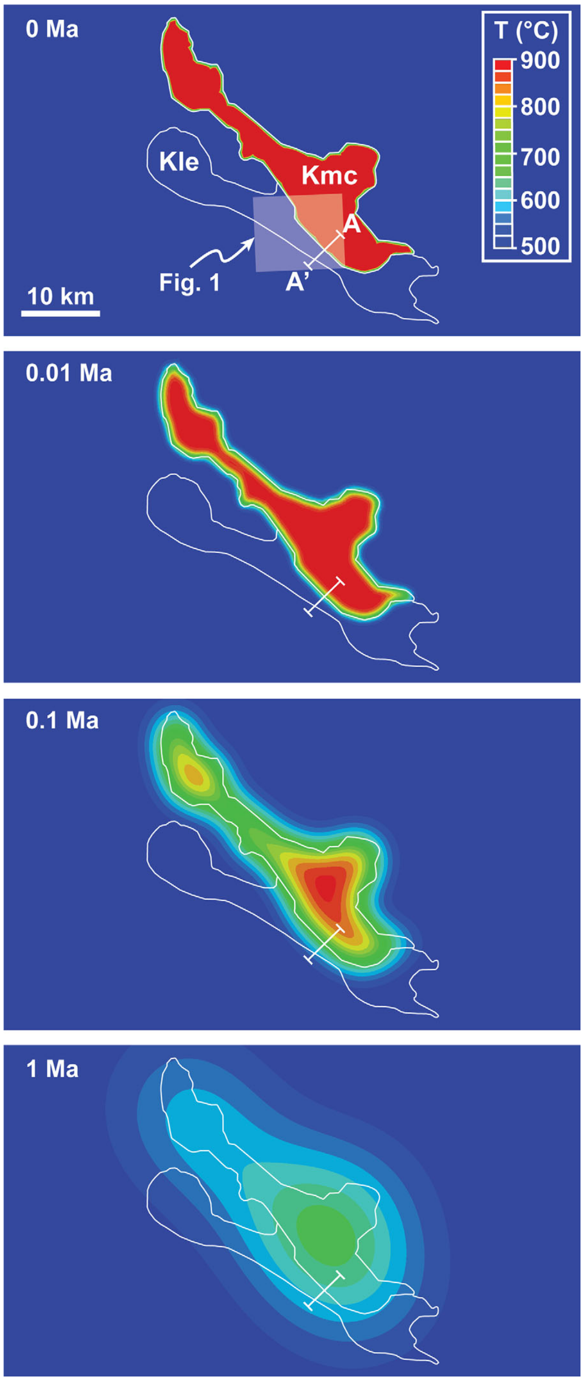

Figure 10. Heat conduction from the Mono Creek pluton (Kmc) into the Lake Edison pluton (Kle) and surrounding areas, as modeled using the finite element method. Results are shown for 0, 0.01, 0.1, and 1 Ma after the intrusion of Kmc at 86 Ma. The 6 km long path A-A′ (also shown in Figure 1) is used to compare model results in Figure 6. The panel for $t=0$ includes the location of the field area map given in Figure 1.

$$\theta = \frac{T - T_0}{T_m - T_0}, \tag{7}$$

where T_0 is the ambient temperature (°C) of the host rock and T_m is the initial temperature of the intrusion. The initial conditions are that at $t=0$, $T=T_m$ for $-a<x<a$ and that $T=T_0$ for $x<-a$ and $x>a$. The boundary condition is that at $x=\infty$, $T=T_0$ for all t.

3.3.2. Validation of Tabular Model Geometry for Mono Creek Pluton

Although plutons within the Mount Abbot Quadrangle are generally tabular in shape, it is not clear that the Mono Creek pluton can be properly characterized as an infinite slab of finite thickness. To test this, we constructed a 2-D finite element model (FEM) that incorporates the cross-sectional shape of the Mono Creek pluton at the current level of erosion and compare the results to the *Lovering* [1935] 1-D analytical solution.

The FEM model was constructed using the Complete Abaqus Environment (https://www.3ds.com/products-services/simulia/products/abaqus/abaquscae/). In the model, the geometry of the Mono Creek pluton was taken from the map included as Figure 2 in *Tikoff and de Saint Blanquat* [1997]. The pluton is placed in the center of a model domain that measures 1000 km × 1000 km, which is large enough to negate any edge effects. The initial conditions are that at time $t=0$, the Mono Creek pluton has a uniform temperature of 900°C, while the host rock has a uniform temperature of 500°C. The temperature 900°C is the approximate closure temperature for the U-Th-Pb system in zircon [*Lee et al.*, 1997], which was used to put constraints on the timing of intrusion of the Mono Creek pluton. The host rock temperature was calculated using a geothermal gradient of 40°C/km at a depth of 12.6 km. The depth of 12.6 km is based on the geobarometric estimate of 315 MPa for the emplacement pressure and a lithostatic pressure gradient of 25 MPa/km. The boundary condition is that at the model periphery, $T=500$°C for all t; the ambient temperature remains constant. Material properties used in all models are reported in Table 2.

FEM results are given in Figure 10 for $t = 0$, $t = 0.01$, $t = 0.1$, and $t = 1$ Ma, indicating time after emplacement of the Mono Creek pluton at 86 Ma. Temperature profiles for sections adjacent to the NW and SE extremities of the pluton are expected to be influenced by edge effects and thus are less likely to be properly characterized by the *Lovering* [1935] geometry. The transect A-A′ from the center of the Mono Creek

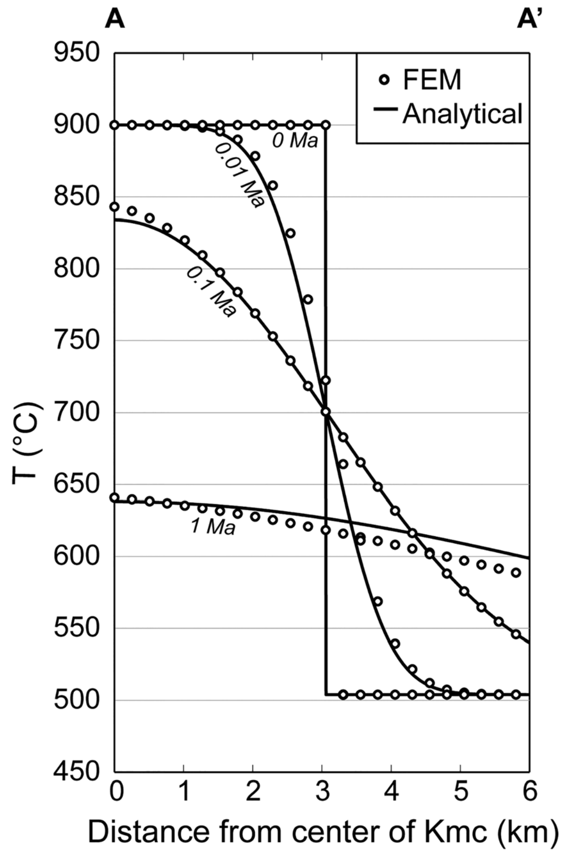

Figure 11. Comparison between the 2-D finite element model results collected along the path A-A' (see Figure 1) and the 1-D analytical solution for heat conduction from an infinite slab of finite thickness. The pluton contact is located at 3.054 km from the center of Kmc.

pluton through the Lake Edison pluton was placed at the southeastern extent of the microstructural sample locations to ensure that these sites are far enough from the pluton termination to be appropriately characterized by the *Lovering* [1935] solution. Along this transect, nodes are spaced every 250 m and record the temperature history over 1 Ma. The results are compared to the analytical solution in Figure 11.

The analytical solution provides an excellent match to the FEM for the first 0.1 Ma, and an acceptable match at 1 Ma. The greatest misfit between the analytical solution and the FEM is 12°C (only 3% of $T_m - T_0$), which occurs at $t = 1$ Ma and $x = 6$ km ($\sim$3 km from the pluton contact). An equivalent misfit previously was deemed acceptable by *Stowell and Pike* [2000] to justify their use of a 1-D numerical model of sill-related heat conduction. The agreement between the FEM and the analytical solution demonstrates that the geometry of the Mono Creek pluton may be idealized as an infinite slab of finite thickness, permitting use of the *Lovering* [1935] analytical solution and other solutions based on that geometry.

While the FEM allows us to evaluate the importance of 1-D versus 2-D analysis in the horizontal plane, thermal variability in the vertical direction also could have a significant effect. The dip of the contact between the Mono Creek and Lake Edison plutons is subvertical, evidenced by its straight trend across the rugged topography ($\sim$700 m elevation change) of the Mount Abbot Quadrangle geologic map [*Lockwood and Lydon*, 1975]. Thus, vertical heat transfer due to a dipping Mono Creek pluton above or below the Lake Edison pluton is unlikely. Furthermore, geobarometry and mantle xenoliths indicate that granitoid plutons may have extended to $\sim$30 km depth during the late Cretaceous [*Ducea and Saleeby*, 1998]. The high aspect ratio of Mono Creek pluton (height-to-width $\sim$6:1) suggests that a 1-D analysis is appropriate as it does not neglect significant out-of-plane effects.

3.3.3. 1-D Analytical Solution With Ambient Temperature Evolution

Using a 1-D analytical solution allows us to incorporate evolving ambient temperature into the analysis. We infer that the ambient temperature in the vicinity of the Mono Creek pluton must have decreased between 86 and 79 Ma due to unroofing and exhumation, in addition to the change from a magmatic arc to a fore-arc setting. Based on Figure 3 and assuming a lithostatic pressure gradient of 25 MPa/km, the depth likely decreased from 12.6 to 10 km between 86 and 79 Ma. Furthermore, the transition from a magmatic arc setting with a high geothermal gradient (40°C/km) to a fore-arc basin setting with a low geothermal gradient (10°C/km) occurred at $\sim$80 Ma. We suggest that a geothermal gradient of 25°C/km is a reasonable estimate for 79 Ma. The result of these changes in depth and geothermal gradient is that the ambient temperature changed from $\sim$500°C at 86 Ma to $\sim$250°C at 79 Ma.

We assume that evolution of the ambient temperature is linear with time and incorporate it into the *Lovering* [1935] solution, as follows:

$$T(t) = \frac{1}{2}[T_m - T_0(t)]\left[\operatorname{erf}\left(\frac{a+x}{2\sqrt{\kappa t}}\right) + \operatorname{erf}\left(\frac{a-x}{2\sqrt{\kappa t}}\right)\right] + T_0(t). \quad (8)$$

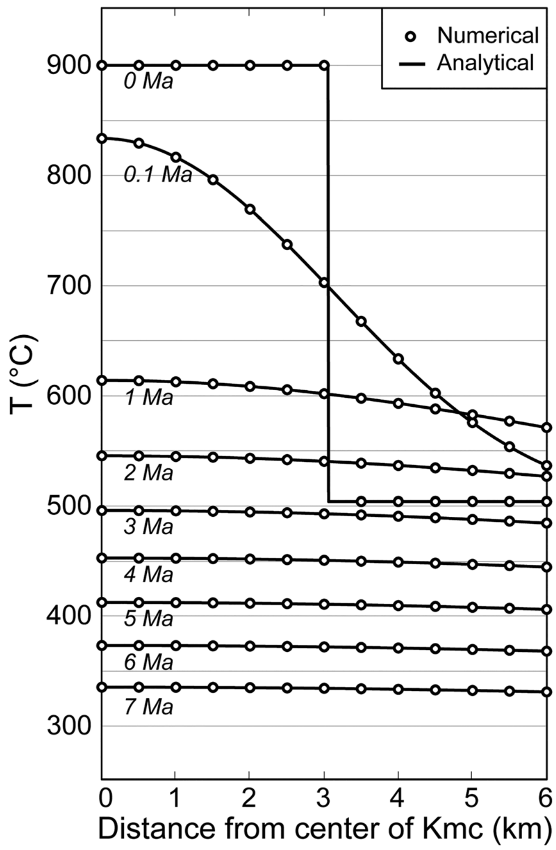

Figure 12. Comparison between 1-D numerical model and the 1-D analytical solution for heat conduction from an infinite slab of finite thickness. Both incorporate evolution of the ambient temperature term.

Using equation (8) and the thermal properties given in Table 2, we obtain results for the range $t = 1$ Ma to $t = 7$ Ma, shown in Figure 12. To ensure that this solution properly incorporates the evolution of the ambient temperature, we also constructed a numerical solution. In the numerical solution, each time step is characterized by a unique ambient temperature, which is constant over that time interval. The ambient temperatures assigned to each time step are consistent with the linear decrease of ambient temperature from 500°C at $t = 0$ to 250°C at $t = 7$ Ma. For each time step, the temperature calculated is the sum of all of the temperatures determined for the previous time intervals:

$$T_n = \sum_{i=1}^{n} T_i - T_{i-1}, \tag{9}$$

where T_n is the temperature at the nth time interval. Correspondence between the analytical and numerical solutions (Figure 12) suggests that the analytical solution appropriately accounts for the changes in ambient temperature. The solution can thus be used to estimate the changes in temperature over much longer time scales (Figure 13).

Published radiometric ages for hornblende, biotite, white mica, and microcline (plotted in Figure 13 and tabulated in supporting information Table S1) are used to evaluate the success of the analytical thermal model (equation (8)) in predicting the cooling history of the Mount Abbot Quadrangle after intrusion of the Mono Creek pluton. The residual, defined as the temperature difference between the radiometric data and the model results, has a mean value of 69 ± 46°C. In addition, the model intersects the error bounds on at least one sample for each mineral type considered, attesting to the model's adequacy over the timescale and temperature range of deformation in the field area. A model incorporating latent heat also was tested (and is provided in the supporting information), but provided a poorer fit to radiometric data, overestimating the temperature by ~170°C at 85 Ma. Thus, the model without latent heat is considered for the remainder of this paper.

3.3.4. Potential Importance of Thermal Convection

The thermal conduction model neglects the potential impact of convective heat transport. Field evidence, including hydrothermal mineral precipitates and alteration zones, indicates that fractures in the Mount Abbot Quadrangle likely served as paleofluid conduits [*Segall and Pollard*, 1983b; *Segall and Simpson*, 1986; *Martel et al.*, 1988; *Christiansen*, 1995]. Convection within these fracture networks may have allowed the plutons to cool more quickly than by conduction alone and may have played a role in the local thermal gradients at the outcrop-scale. *Christiansen* [1995] found that biotite samples collected in outcrops that were densely fractured and hydrothermally altered yielded younger $^{40}Ar/^{39}Ar$ ages (by ~2 Ma), in comparison to samples collected in areas devoid of fractures and evidence for hydrothermal alteration

Table 2. Material Properties

ρ (kgm^{-3})	2648[a]
k (Wm^{-1}K^{-1})	2.13[b]
c_p (Jkg^{-1}K^{-1})	1046[c]
κ (m^{2}s^{-1})	7.7×10^{-7} [d]
L (Jkg^{-1})	2.1×10^{-5} [e]
λ_2	0.41
t_s (Ma)	2.3×10^{-7}

[a] *Morrow and Lockner* [2006].
[b] Consistent with *Whittington et al.* [2009].
[c] *Mel'nikova et al.* [1975].
[d] *Durham et al.* [1987].
[e] *Fyfe* [1973].

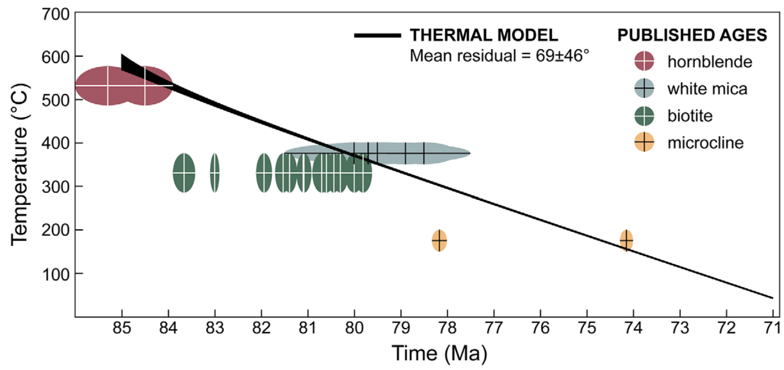

Figure 13. Results of the 1-D heat conduction model that incorporates ambient temperature evolution, along with published individual radiometric ages for hornblende ($T_c = 530 \pm 45°C$) [*Harrison*, 1981], biotite ($T_c = 330 \pm 45°C$) [*Grove and Harrison*, 1996], white mica (T_c = 350–400°C) [*Xu et al.*, 2000; *Hames and Bowring*, 1994; *Wagner et al.*, 1977], and microcline (T_c =150–200°C) [*Shaw et al.*, 1999]. Supporting information Table S1 contains locations, numerical values, and references for the data presented in this figure [*Bergbauer and Martel*, 1999; *Christiansen*, 1995; *Segall et al.*, 1990; *Pachell and Evans*, 2002]. Model results are shown as an uncertainty envelope, constrained by the temperature calculated for the sample location closest to the Kle-Kmc contact and the sample location furthest from the Kle-Kmc contact. Thus, the envelope illustrates the possible range of temperature within the sampled region. Radiometric ages that precede intrusion of the Mono Creek pluton have been omitted from this figure. For hornblende and biotite samples, ellipses represent uncertainty of one mean standard deviation for both the age and closure temperature. For white mica and microcline samples, ellipses represent uncertainty of one standard deviation in the age and the reported range of closure temperatures for those minerals. Residuals were calculated as the difference in temperature between the radiometric data and the model results. The mean and standard deviation of the residuals (neglecting outliers $>2\sigma$) are reported for the model.

(supporting information Table S1). This suggests that circulation of hydrothermal fluids allowed fractured regions to remain hot over longer time periods than intact regions. Thus, convection of hot fluids within fracture networks likely played a role in the cooling history of the field area. Had the thermal model incorporated convection, it would have predicted a faster cooling rate and may have provided a better fit to the radiometric data.

4. Discussion

4.1. Microstructural Evidence for Decreasing Temperature During Deformation

Microstructural observations indicate that temperature likely decreased during deformation and progressive strain localization. This is in contrast to the conclusion of *Bestmann and Pennacchioni* [2015] that the fabric of their “protolith,” “protomylonite,” and “mylonite” samples developed at a constant temperature. The samples analyzed in their study came from a single outcrop within the Rosy Finch Shear Zone, at the border between the Lake Edison and Mono Creek plutons (G. Pennacchioni, personal communication, 2015, Figure 1). Photomicrographs and pole figures presented in their paper indicate right-lateral shear, in contrast to the majority of left-lateral faults and shear zones within the Lake Edison granodiorite, including all of the fault-related samples analyzed in this study.

An important factor that contributed to the conclusion of *Bestmann and Pennacchioni* [2015] of constant deformation temperature was their interpretation that the shear zones, which nucleated along preexisting joints and dikes, widened over time. However, fault-related samples in the current study were collected not along the fault itself, but within strongly foliated granodiorite adjacent to fault tips or within fault steps. In these regions, there is evidence for strain localization with time, including the observation that fault arrays with greater offset have stronger fabrics at fault tips and steps [*Nevitt*, 2015]. Moreover, mechanical modeling of fault steps shows that as displacement accrues, the gradient in shear strain across the step increases (i.e., strain localizes) [*Nevitt*, 2015]. Thus, for shear zones adjacent to fault tips, the highly deformed zone in the center likely represents the latest stage of deformation.

Another argument made by *Bestmann and Pennacchioni* [2015] for constant deformation temperature is their assertion that the shear zones developed in a very short-time period (<1 Ma), based on a radiometric age date for hornblende of 89.1 ± 1.1 Ma in the Lake Edison granodiorite [*Davis et al.*, 2012]. This neglects the analyses by *Bergbauer and Martel* [1999], which yielded hornblende ages ranging from 85.3 ± 0.7 Ma to 88.7 ± 0.4 in the Lake Edison granodiorite. Moreover, it assumes that all deformation occurred at a temperature greater than the closure temperature of hornblende, 490–580°C [*Harrison*, 1981], though deformation may have occurred at lower temperatures. Biotite ages corresponding to a closure temperature of 280–345°C [*Harrison et al*., 1985] are significantly younger in the Lake Edison granodiorite (~80 Ma, supporting information Table S1). In addition, two independent studies [*Segall et al*., 1990; *Pachell and Evans*, 2002] concluded that faults remained active until ~79 Ma, based on radiometric ages of white mica that grew in association with the faults. Thus, fault-related ductile shear zones likely remained active for more than 1 Ma, and possibly up to 9 Ma in the Lake Edison granodiorite, assuming a crystallization age of 88 Ma [*Tobisch et al*., 1995].

Our conclusion that temperature decreased during deformation is based on the occurrence of both high- and low-temperature synkinematic mineral assemblages that most likely did not form coevally. Microstructural evidence for high-temperature (400–500°C) deformation includes myrmekite, feldspar plasticity, prism-<a> slip in quartz, and GBM recrystallization in quartz. Evidence for shear zone deformation at low-temperatures (<350°C) includes kinked and fractured biotite grains, in addition to chlorite and epidote growing within pressure shadows of porphyroclasts and within feldspar pull-aparts. Furthermore, chlorite-after-biotite and pervasive sericite suggest that hydrothermal fluids continued to alter the granodiorite at low-temperatures, possibly postdeformation, in both fault-related and regional samples. Zeolite veins, which crosscut all deformation features, further attest to low-temperature alteration [*Griffith et al*., 2008].

In all examined samples from the Lake Edison granodiorite, quartz CPOs indicate the prism-<a> slip system [*Griffith et al*., 2008; *Bestmann and Pennacchioni*, 2015; this study]. However, once the Y-maximum CPO was established at a high-temperature, quartz c-axes would have been poorly oriented for lower-temperature basal-<a> slip [*Toy et al*., 2008]. Particularly in regions subjected to greater shear strain, the prism-<a> slip system may have remained active at temperatures <400°C and thus may not be a reliable indicator of temperature in the fault-related samples.

4.2. Partial Ti Reequilibration During Recrystallization

A growing body of literature suggests that Ti reequilibration during quartz recrystallization often is heterogeneous and incomplete, particularly at lower temperatures [e.g., *Kidder et al*., 2013; *Ashley et al*., 2014; *Bestmann and Pennacchioni*, 2015]. For the Lake Edison granodiorite, we find that Ti likely was reequilibrated in the higher-temperature regional samples, but not in the lower-temperature fault-related samples.

Within the regional samples, Ti concentrations and distributions suggest reequilibration during deformation at a temperature below the granodiorite solidus. Regional samples were significantly deformed at a relatively high-temperature, evidenced by the moderately strong quartz CPO and microstructures indicating GBM and SGR recrystallization (Figure 4). Based on the occurrence of a pervasive regional foliation throughout the pluton, the entire Lake Edison granodiorite underwent this deformation. Experiments have shown that Ti concentrations reset during high-temperature recrystallization [e.g., *Nachlas and Hirth*, 2015]. To evaluate whether this was the case for the Lake Edison granodiorite, we compare Ti content in the regional samples to measurements made in other, undeformed granodiorites similar in composition. For example, a medium-grained biotite-amphibole granodiorite from the Central Bohemian Pluton (Czech Republic) yielded [Ti] in quartz ranging from 49 to 143 ppm, with an average of 87 ppm [*Breiter et al*., 2013]. Similarly, quartz in the Alta Stock granodiorite (Utah) has [Ti] in the range 55–105 ppm, with an average of 75 ppm [*Johnson*, 2009]. In the Lake Edison granodiorite, the 10 measurements corresponding to the upper 5% of the data have an average [Ti] of 53 ppm, well below the average [Ti] in the undeformed Central Bohemian and Alta Stock granodiorites. Thus, quartz in the Lake Edison granodiorite does not appear to have retained the Ti concentration of the magmatic protolith. Furthermore, the lack of correlation between Ti content and grain size (Figure 7) or distance to grain boundaries suggests that Ti approximately reset to an equilibrium concentration during this early deformation.

Ti distribution in the fault-related samples, however, suggests that Ti content only partially reequilibrated during localized deformation, in agreement with the results of *Bestmann and Pennacchioni* [2015] for an outcrop in the field area. The distribution of Ti is heterogeneous in fault-related samples, with bands of lower and higher Ti content that anastomose with the foliation (Figure 8). Because we were unable to determine whether the lowest-Ti analyses represented equilibrium values, temperature estimates based on TitaniQ in the fault-related samples may overestimate the true deformation temperature.

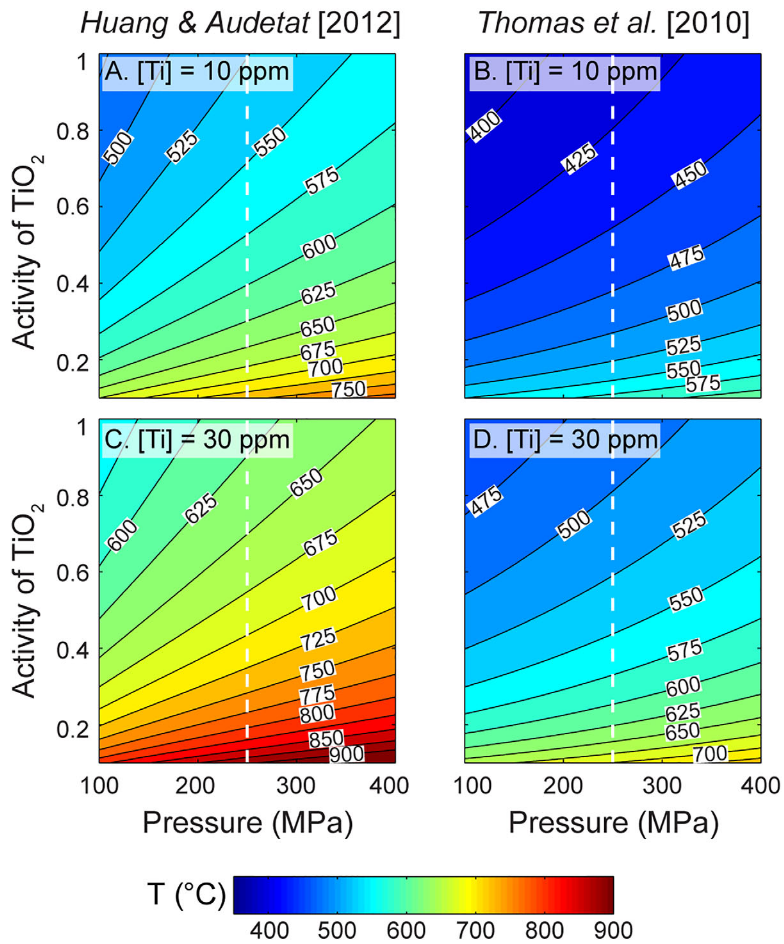

Figure 14. Variation in temperature due to uncertainty in confining pressure (100–400 MPa), TiO_2 activity (0.1–1), and calibration choice. The *Huang and Audétat* [2012] calibration was used to calculate temperature in plots (a) and (c), while the *Thomas et al*. [2010] calibration was used in plots (b) and (d). Plots (a) and (b) assume [Ti] = 10 ppm, representative of fault-related samples, while plots (c) and (d) assume [Ti] = 30 ppm, representative of regional samples. The white-dashed line indicates P = 250 MPa, the lithostatic pressure used in TitaniQ calculations reported in the remainder of this paper.

4.3. TiO_2 Activity: A Major Uncertainty in TitaniQ Thermobarometry

Estimating TiO_2 activity (a_{TiO_2}) is a source of significant uncertainty for temperature estimates made using TitaniQ, regardless of which calibration is used. Most estimates of TiO_2 activity in granitoids range from 0.6 to 1.0 [*Ghent and Stout*, 1984; *Wark and Watson*, 2006; *Wark et al*., 2007; *Kohn and Northrup*, 2009; *Behr* and *Platt*, 2011]. In contrast, *Bestmann and Pennacchioni* [2015] concluded that TiO_2 activity in the Lake Edison granodiorite was significantly lower, either $<$0.1 or $\sim$0.25 depending on the TitaniQ calibration used. This estimate is derived from their conclusion that the temperature remained constant at 500°C, even as quartz infilled feldspar pull-aparts and pressure shadows with [Ti] = 2 ppm. However, numerous examples occur both in our study and theirs (i.e., SOM-Figure 1) [*Bestmann and Pennacchioni*, 2015] of feldspar fractures, pull-aparts, and pressure shadows filled with quartz $\pm$ epidote $\pm$ chlorite (Figures 4e, 5i–5k), suggesting that low [Ti] in those regions may correspond to a temperature closer to 350°C. Thus, we find the *Bestmann and Pennacchioni* [2015] activity estimate to be unrepresentative, though some pull-aparts may have formed at higher temperature.

Uncertainty in activity, confining pressure, and calibration choice can produce a wide range of possible temperatures for a given concentration of Ti (Figure 14), which significantly limits the utility of TitaniQ thermobarometry for providing quantitative temperature estimates. To demonstrate this, we calculated temperature as a function of TiO_2 activity and pressure using both the *Huang and Audétat* [2012] and *Thomas et al*. [2010] calibrations. Figure 14 illustrates the resulting temperature variability calculated using [Ti] = 10 ppm (Figures 14a and 14b) and 30 ppm (Figures 14c and 14d), concentrations representative of fault-related and regional samples, respectively. The range of TiO_2 activity (0.1–1.0 ppm) and confining pressure (100–400 MPa; Figure 3) used in Figure 14 correspond to uncertainties in those parameters for the Lake Edison granodiorite during deformation. For each value of [Ti], the *Huang and Audétat* [2012] calibration corresponds to a greater range of possible temperatures (320°C at 10 ppm; 390°C at 30 ppm) than does the *Thomas et al*. [2010] calibration (230°C at 10 ppm; 290°C at 30 ppm). The possible temperature range increases with increasing Ti content for both calibrations. Importantly, even if pressure is known (e.g., dashed white lines in Figure 14), significant uncertainty in TiO_2 activity results in a $>$175°C range of possible temperatures, plus a $\sim$200°C difference depending on which calibration is chosen.

We place constraints on the minimum TiO_2 activity for this study through back-calculation using [Ti] measurements made in the Lake Edison granodiorite and a typical crystallization temperature for granitic rocks of $\sim$785°C [*Maaløe and Wyllie*, 1975]. Because Ti likely reequilibrated in quartz after a period of cooling post-crystallization, we expect the upper 5% of data (average [Ti] = 53 ppm) to underestimate the true magmatic Ti concentration. Thus, equating 53 ppm to 785°C and solving for a_{TiO_2} yields a *minimum* bound on activity. Assuming the emplacement confining pressure of 315 MPa, minimum activity estimates calculated using the *Huang and Audétat* [2012] and *Thomas et al*. [2010] calibrations are $a_{TiO_2} = 0.45$ and $a_{TiO_2} = 0.11$, respectively. For comparison, if we input [Ti] = 80 ppm, representative of the undeformed Alta Stock granodiorite [*Johnson*, 2009] and Central Bohemian Pluton [*Breiter et al*., 2013], the estimated activities are $a_{TiO_2} = 0.68$ and $a_{TiO_2} = 0.16$ for the *Huang and Audétat* [2012] and *Thomas et al*. [2010] calibrations, respectively. As the maximum bound for TiO_2 activity is unknown, we followed the example of previous studies in sphene-bearing granitoids [*Kohn and Northrup*, 2009; *Behr and Platt*, 2011; *Nadin et al*., 2016] and assumed $a_{TiO_2} = 0.8$ to produce Figure 9.

The above calculations assume that TiO_2 activity remained spatially uniform and did not change over time during cooling [cf., *Ashley and Law*, 2015]. While these assumptions are routinely made, our observations and other recent work indicate more variable behavior that also limits the utility of the TitaniQ thermobarometer. For example, Figures 8a and 8b clearly show that resetting of Ti was not uniform along all grain boundaries (see also *Bestmann and Pennacchioni*, 2015, Figure 5a). In addition, Figure 8 suggests that TiO_2 activity was lower adjacent to Ti-rich phases (i.e., biotite and sphene), similar to previous observations in quartz-rich rocks [e.g., *Nachlas et al*., 2014]. At distances greater than $\sim$100 μm from biotite and sphene, preexisting Ti in neighboring quartz grains may have buffered TiO_2 activity. Other explanations for nonuniform Ti reequilibration include heterogeneous dislocation densities, or intergranular fluids with pressure, temperature, or composition-dependent Ti solubility [*Nachlas and Hirth*, 2015].

Overall, we conclude that relative differences in Ti concentrations can provide useful constraints on relative temperature differences during deformation [e.g. this study; *Cross et al*., 2015]. Our study suggests, however, that TitaniQ, at present, is not a dependable method for quantitatively constraining the temperature of quartz recrystallization. As such, our conclusions below are based on trends in Ti content and do not depend on temperatures calculated through TitaniQ.

4.4. Timing of Jointing, Faulting, and Fabric Development During Pluton Cooling

Combined with the heat conduction model, microstructural relationships and TitaniQ data place constraints on the timing of various deformation events within the Lake Edison granodiorite (Figure 15). Samples for microstructural and TitaniQ analyses were collected at outcrops that vary in elevation by approximately 500 m (Table 1), which corresponds to a temperature variability of 20°C assuming a geothermal gradient of 40°C/km. Although the samples do not align with a perfectly one-dimensional transect, the error associated with elevation variability is within the uncertainty of the microstructural constraints on temperature and on the order of the mean standard deviation associated with [Ti] measurements (Table 1 and Figure 9).

Microstructural constraints indicate a temperature range of 400–500°C for the mylonitic deformation (grey box in Figure 15), which corresponds to approximately 83–81 Ma in the thermal model. For each outcrop, TitaniQ results indicate that the regional foliation developed at a higher temperature than did the fault-related foliation. We conclude from this that the regional foliation developed first at a higher temperature, while faulting and fault-related ductile deformation occurred later following a period of cooling. These results are consistent with the conclusions of *Christiansen* [1995], who found that, on average, biotite grains within mylonitized granodiorite in fault steps yielded younger $^{40}Ar/^{39}Ar$ ages than biotite grains within the regional foliation (supporting information Table S1). *Christiansen* [1995] suggests that mechanical

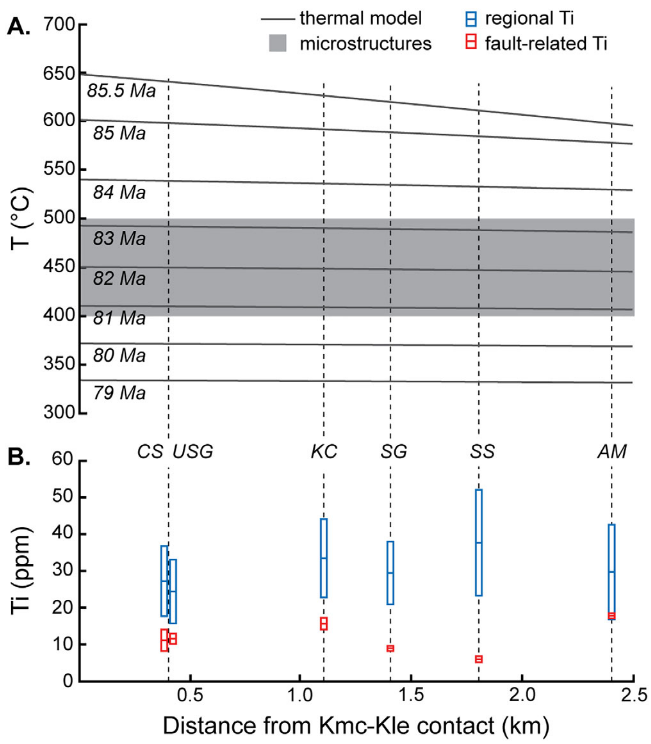

Figure 15. Summary of results of thermal model, microstructural analysis, and TitaniQ analysis. (a) 1-D analytical solution for conduction from 85.5 to 79 Ma with microstructural constraints for the high-temperature foliation (400–500°C) marked by the grey box. (b) TitaniQ results, with each rectangle indicating one standard deviation greater than and less than the mean value for the outcrop.

deformation of biotite grains in fault steps reset the $^{40}Ar/^{39}Ar$ systematics. Other evidence for deformation continuing to lower temperatures include the occurrence of lower greenschist facies minerals, cataclasites, and pseudotachylytes within faults [*Martel et al.*, 1988; *Griffith et al.*, 2008; *Griffith et al.*, 2009a; *Kirkpatrick and Shipton*, 2009; *Kirkpatrick et al.*, 2009].

Constraining the timing of fault-related fabric development leads to a more precise estimate of joint formation and faulting than previously has been reported. The formation of joints and their subsequent re-activation as faults must have preceded the development of the fault-related fabrics at ~83 Ma (Figure 15). Joints in the Bear Creek region typically contain lower greenschist minerals, primarily chlorite and epidote, with minor amounts of calcite, muscovite, sericite, and zeolite [*Segall and Pollard*, 1983a]. The presence of this mineral assemblage led others [e.g. *Bergbauer and Martel*, 1999] to conclude that jointing must have occurred after the pluton cooled to a temperature <570°C, which corresponds to ~85 Ma in Figure 13. Thus, jointing and initial faulting likely occurred between ~85 and 83 Ma. *Pennacchioni and Zucchi* [2013] suggest that 570°C overestimates the temperature corresponding to the joint mineral assemblage. In that case, either 85 Ma overestimates the age of joint formation, or lower greenschist minerals within joints represent a later stage of deformation.

In summary, our analysis supports the hypothesis that intrusion of the Mono Creek pluton at 86 Ma reheated the Lake Edison pluton, which continued to cool during deformation. Thermal modeling of the intrusion and subsequent conduction predicts a thermal history that is generally consistent with radiometric age data from the field area (Figure 13). Following intrusion, a set of cooling joints developed that later were reactivated as left-lateral faults between ~85 and 83 Ma. Fault slip resulted in mylonitization of granodiorite within contractional quadrants of fault tips and contractional fault steps. Based on microstructural evidence, both within contractional steps (e.g., kinked biotite grains) and faults (e.g., epidote-rich cataclasite), deformation continued at temperatures below ~350°C. However, the pattern of brittle and ductile features is not distributed homogeneously throughout the field area, suggesting that different stages of deformation may have focused in certain locations.

4.5. Duration of Spatial Temperature Gradient Following Intrusion

Conductive heat transfer following pluton emplacement is expected to produce a spatial gradient in temperature that radiates away from the intrusion (e.g., Figure 10). The longevity of such a temperature gradient associated with intrusion of the Mono Creek pluton and its impact on the distribution of structural features within the Lake Edison granodiorite has been the subject of some debate. *Bürgmann and Pollard* [1994] recognized that ductile deformation features become increasingly prominent with decreasing distance from the Mono Creek pluton contact. Faults located in outcrops further from the pluton contact (blue in Figure 2; e.g., Bear Creek Meadows) [*Griffith et al.*, 2009b] generally exhibit more brittle features, including cataclasite, wing cracks, and rhombochasms, with relatively weak ductile fabric development compared to other outcrops in the field area. In outcrops located closer to the pluton contact (red in Figure 2; e.g., Seven Gables outcrop) [*Nevitt et al.*, 2014], faults commonly are accompanied by strong mylonitization with less prominent secondary fracturing. Note, however, that most outcrops throughout the pluton exhibit some degree of both mylonitization and fracturing [*Pennacchioni and Zucchi*, 2013; this study].

In addition, *Bürgmann and Pollard* [1994] observed that the ductile fabric distribution around fault tips becomes symmetric for faults located closest to the Mono Creek pluton. Based on these observations and mechanical modeling, they hypothesized that the temperature gradient associated with intrusion of the Mono Creek pluton persisted at the time of faulting, concentrating higher-temperature ductile deformation near the pluton contact. In contrast, *Pennacchioni and Zucchi* [2013] observed that the mechanisms of strain accommodation associated with faulting remained approximately constant throughout the pluton, which might suggest that any intrusion-related temperature gradient had dissipated by the time of faulting. However, *Pennacchioni and Zucchi* [2013] also note heterogeneous deformation throughout the pluton, with greater fault displacement and ductile strain focused near the pluton contact, which they hypothesized could be due to longer-lasting high temperatures there.

The thermal conduction model and Ti data directly test the hypothesis of a temperature gradient during deformation. The model indicates that intrusion of the Mono Creek pluton at 86 Ma created a steep temperature gradient across the Lake Edison pluton only during the first $\sim$1 Ma following intrusion. However, by 85 Ma, the temperature gradient across the pluton had decreased to $<$10°C/km and by 84 Ma, the gradient had decreased to $<$5°C/km (Figure 15). Thus, it is unlikely that a temperature gradient across the pluton is responsible for the apparent prevalence of ductile deformation closer to the Mono Creek pluton. The TitaniQ results (Figure 15) provide further evidence that a systematic temperature gradient did not exist across the Lake Edison pluton at the time of deformation in these samples. Interpreted more broadly, the thermal model and Ti data presented here suggest that the spatial temperature gradient associated with granitic pluton intrusion in arc settings may be relatively short-lived ($<$1 Ma).

4.6. Spatial and Temporal Partitioning of Brittle and Ductile Deformation During Pluton Cooling

In the absence of a temperature gradient, the apparently heterogeneous distribution of dominantly brittle versus ductile deformation in the Lake Edison granodiorite is enigmatic. Here, we explore possible impacts of several kilometer-scale structures on the mode of deformation, including the Rosy Finch Shear Zone [e.g., *Tikoff et al*., 1998], the fluid-rich contact between the Lake Edison and Mono Creek plutons, and the kilometer-scale Bear Creek Kink Band [*Davies and Pollard*, 1986; *Pachell et al*., 2003].

The Rosy Finch Shear Zone (Figure 2) likely initiated during emplacement of the Mono Creek pluton and remained active until $\sim$80 Ma [*Tikoff and Teyssier*, 1992]. Because our findings suggest that the joints were reactivated as faults at $\sim$83 Ma, the Rosy Finch Shear Zone may be kinematically related to these faults. Development of the shear zone has been attributed to a transpressional stress regime [*Tikoff and Teyssier*, 1992], which may have exploited preexisting joints that were oriented for left-lateral slip. Although this provides an explanation for fault initiation in the field area, it does not account for the variation in structural style.

The prevalence of ductile deformation near the contact with the Mono Creek pluton could be due to the relative abundance of fluids there, as suggested by the concentration of aplite and pegmatite dikes in that region [*Christiansen*, 1995; *Pennacchioni and Zucchi*, 2013]. Because these dikes are associated with late stage, fluid-rich magmatism, the pluton contact may represent a fluid-rich region that enabled local water weakening and enhanced crystal plasticity. This is analogous to the water weakening mechanism described by *Kronenberg et al*. [1990] at the outcrop-scale in the Lake Edison granodiorite. At the kilometer-scale, elevated fluid concentrations near the pluton contact may account for increased ductility in that region. Moreover, enhanced water weakening at pluton contacts could explain strain localization at a much larger-scale, such as the Sierra Crest Shear Zone, which spans the axis of the Sierra Nevada Batholith, and often coincides conspicuously with pluton contacts [e.g., *Tikoff and de Saint Blanquat*, 1997].

The kilometer-scale Bear Creek Kink Band provides another explanation for the distribution of structures in the field area. Figure 2 shows the major lineations in the southern half of the Mount Abbot Quadrangle [*Lockwood and Lydon*, 1975], the axial traces of the Bear Creek Kink Band [*Davies and Pollard*, 1986; *Pachell et al*., 2003], and the locations of representative outcrops previously studied in the Lake Edison granodiorite. These outcrops are categorized qualitatively based on the relative abundance of brittle features (i.e., wing cracks, cataclasis, rhombochasms), and ductile features (i.e., mylonitic foliation), though most outcrops contain both brittle and ductile features. Interestingly, outcrops characterized by more prominent brittle and dynamic (i.e., pseudotachylyte) structures occur near an axial trace of the kink band, while outcrops dominated by ductile deformation occur within the limb of the kink band. These observations are the basis for our new hypothesis regarding the relationship between the Bear Creek Kink Band and the variation in deformation mode within the Lake Edison granodiorite.

Kink bands form by slip on closely spaced planar discontinuities, which are provided by left-lateral faults within the Mount Abbot Quadrangle. The faults bend along the kink band hinges and rotate within the kink band relative to the faults outside the kink band. According to this conceptual model, right-lateral displacement across the Bear Creek Kink Band occurred after initial slip on the faults. Thus, initial fault slip likely occurred at a relatively high temperature (400–500°C), which resulted in the mylonitic fabrics observed within fault steps and near fault tips. The plutons cooled and some faults continued to slip as the Bear Creek Kink Band developed. While kink band deformation progressed and the plutons cooled to lower temperatures ($\sim$350°C), we hypothesize that deformation focused near the kink band hinges. At lower temperatures, faulting there resulted in the development of abundant wing cracks, cataclasite, and in some cases, pseudotachylyte.

At the kilometer-scale, *Pennacchioni and Zucchi* [2013] note an increase in the total accumulated offset and greater host rock (ductile) deformation for faults located near the pluton contact and within the Rosy Finch Shear Zone. Their study primarily looked at the East Fork and Hilgard Creeks (see Figure 1), which intersect the Rosy Finch Shear Zone near the center of the Bear Creek Kink Band. For meter-scale kink bands that contain slip indicators [e.g., Figure 1 of *Martel*, 1999], slip is generally greatest in the center of the kink band. If meter-scale constraints on displacement distributions are applicable at the kilometer-scale, then the greater offset and ductile deformation observed by *Pennacchioni and Zucchi* [2013] may be a result of the Bear Creek Kink Band.

Thus, it appears that a regional kink band may have played a significant role in the temporal and spatial distribution of structures within the Lake Edison granodiorite, and may be an important factor in deformation partitioning in other field areas, as well. For instance, curved lineaments mapped in the Mount Pinchot Quadrangle (central Sierra Nevada) [*Moore*, 1963] and paleomagnetic measurements within the Tehachapi Mountains (southern Sierra Nevada) [*Wood*, 1997] may be diagnostic of additional kink-band examples. Furthermore, regional kink band structures have been observed outside the Sierra Nevada, such as in the transpressive Columbian Andes [*MacDonald et al*., 1996]. Thus, regional kink bands may be an important mechanism of arc-related deformation, particularly in cooling settings where temperature and rheology evolves over time.

5. Conclusions

This study provides new constraints on the evolving temperature and deformation history of the Lake Edison pluton through a combination of microstructural analysis, titanium-in-quartz thermobarometery (TitaniQ), and 1-D heat conduction modeling. Microstructural analysis of mylonitized granodiorite adjacent to faults indicates progressive deformation during pluton cooling, beginning at 400–500°C and continuing to $<$350°C. In addition, TitaniQ reveals a systematic trend of lower Ti content within fault-related samples compared to regional samples, suggesting quartz recrystallization within fault-related samples occurred at a lower temperature. Though useful for assessing these relative [Ti] differences, we conclude that TitaniQ does not yield meaningful temperature estimates, due to partial reequilibration of Ti in quartz, along with significant uncertainty in TiO_2 activity and calibration choice. The thermal model, which predicts a cooling trend consistent with radiometric age data for the area, suggests that intrusion of the Mono Creek pluton at 86 Ma created a steep temperature gradient across the Lake Edison pluton only during the first $\sim$1 Ma following intrusion. During subsequent jointing and faulting (85-79 Ma), the temperature was fairly uniform across the Lake Edison pluton, with average values decreasing during deformation from 585°C at 85 Ma to 332°C at 79 Ma. Thus, heterogeneous deformation across the Lake Edison pluton is not due to a persistent temperature gradient.

We consider three regional structures that may have contributed to the nonuniform distribution of dominantly brittle and ductile structures throughout the pluton: the Rosy Finch Shear Zone, the contact between the Lake Edison and Mono Creek plutons, and the Bear Creek Kink Band. Particularly intriguing is the correlation between deformation styles and geometry of the Bear Creek Kink Band. Outcrops containing dominantly brittle and/or dynamic features (i.e., cataclasite and/or pseudotachylyte) preferentially occur near the axial trace, while outcrops featuring prominent ductile features (i.e., mylonitization of granodiorite) occur within the central limb. These observations suggest that the Bear Creek Kink Band began to develop during the initial stage of faulting, which occurred at 400–500°C. As the pluton cooled, deformation transitioned from dominantly ductile to brittle behavior, which was focused along the axial trace of the regional kink band, continuing to temperatures of <350°C. Future studies can test this hypothesis by constructing mechanical models of kink band development under evolving thermal conditions. Regional kink bands, which are observed elsewhere in the Sierra Nevada and in other transpressive settings, may represent a mechanism for producing spatially heterogeneous deformation in cooling plutons.

Acknowledgments
We thank Whitney Behr and Thorsten Becker for constructive reviews that improved this manuscript. We also thank Ashley Griffith, Libby Ritz, Meredith Townsend, Betsy Madden, Mark McClure, Michael Pollard, Nick Tokach, Tanvi Chheda, and Emily Nevitt for their assistance in the field. Steve Martel and Stephan Bergbauer are thanked for providing radiometric data from Bergbauer's MS thesis. In addition, we are grateful to Paul Segall for preserving his Kip Camp samples and field notes so that they could be used in this study. We also thank Matt Coble for guiding us in the preparation of the TitaniQ samples and Nik Deems for his assistance in the EBSD laboratory. Kathy Barton and the Barton Laboratory are thanked for access to their SEM facility, which is supported by the Department of Plant Biology, Carnegie Institution of Washington. Josie Nevitt was supported by a National Science Foundation Graduate Research Fellowship during this research project. Additional funding was provided by a Stanford McGee Research Grant and the Stanford Rock Fracture Project. Jessica Warren was supported by the National Science Foundation under Grant Number EAR-1347696. Steven Kidder was supported by the National Science Foundation under grant 1064805. TitaniQ data are available in the Supporting Information and samples are available upon request to the corresponding author.

References

Ague, J. J., and G. H. Brimhall (1988), Magmatic arc asymmetry and distribution of anomalous plutonic belts in the batholiths of California: Effects of assimilation, crustal thickness, and depth of crystallization, *Geol. Soc. Am. Bull.*, *100*(6), 912–927.

Ashley, K. T., and R. D. Law (2015), Modeling prograde TiO2 activity and its significance for Ti-in-quartz thermobarometry of pelitic metamorphic rocks, *Contrib. Mineral. Petrol.*, *169*, 23.

Ashley, K. T., L. E. Webb, F. S. Spear, and J. B. Thomas (2013), P-T-D histories from quartz: A case study of the application of the TitaniQ thermobarometer to progressive fabric development in metapelites, *Geochem. Geophys. Geosyst.*, *14*, 3821–3843, doi:10.1002/ggge.20237.

Ashley, K. T., W. D. Carlson, R. D. Law, and R. J. Tracy (2014), Ti resetting in quartz during dynamic recrystallization: Mechanisms and significance, *Am. Mineral.*, *99*(10), 2025–2030.

Babaie, H. A., and T. E. La Tour (1994), Semibrittle and cataclastic deformation of hornblende-quartz rocks in a ductile shear zone, *Tectonophysics*, *229*(1-2), 19–30.

Barton, M. D., and R. B. Hanson (1989), Magmatism and the development of low-pressure metamorphic belts: Implications from the western United States and thermal modeling, *Geol. Soc. Am. Bull.*, *101*(8), 1051–1065.

Bateman, P. C. (1992), Plutonism in the central part of the Sierra Nevada Batholith, California, U.S. Geol. Surv. Prof. Pap., *1483*, 1–186.

Behr, W. M., and J. P. Platt (2011), A naturally constrained stress profile through the middle crust in an extensional terrane, *Earth Planet. Sci. Lett.*, *303*(3-4), 181–192.

Bergbauer, S. (1998), Testing a thermal stress origin of fractures in plutons of the Sierra Nevada batholith, MS thesis, 103 pp., Univ. of Hawaii, Manoa.

Bergbauer, S., and S. J. Martel (1999), Formation of joints in cooling plutons, *J. Struct. Geol.*, *21*(7), 821–835.

Berger, A., and H. Stünitz (1996), Deformation mechanisms and reaction of hornblende: Examples from the Bergell tonalite (Central Alps), *Tectonophysics*, *257*(2–4), 149–174.

Bestmann, M., and G. Pennacchioni (2015), Ti distribution in quartz across a heterogeneous shear zone within a granodiorite: The effect of deformation mechanism and strain on Ti resetting, *Lithos*, *227*, 37–56.

Blackwell, D. D., J. L. Steele, S. Kelley, and M. A. Korosec (1990), Heat-flow in the state of Washington and thermal conditions in the Cascade Range, *J. Geophys. Res.*, *95*(B12), 19,495–19,516.

Brady, R. J., M. N. Ducea, S. B. Kidder, and J. B. Saleeby (2006), The distribution of radiogenic heat production as a function of depth in the Sierra Nevada Batholith, California, *Lithos*, *86*(3-4), 229–244.

Breiter, K., L. Ackerman, M. Svojtka, and A. Müller (2013), Behavior of trace elements in quartz from plutons of different geochemical signature: A case study from the Bohemian Massif, Czech Republic, *Lithos*, *175*, 54–67.

Burchfiel, B. C., and G. A. Davis (1975), Nature and controls of cordilleran orogenesis, western United States: Extensions of an earlier synthesis, *Am. J. Sci.*, *A275*, 363–396.

Bürgmann, R., and D. D. Pollard (1992), Influence of the state of stress on the brittle-ductile transition in granitic rock: Evidence from fault steps in the Sierra Nevada, California, *Geology*, *20*(7), 645–648.

Bürgmann, R., and D. D. Pollard (1994), Strain accommodation about strike-slip fault discontinuities in granitic rock under brittle-ductile conditions, *J. Struct. Geol.*, *16*(12), 1655–1674.

Chapman, A. D., J. B. Saleeby, D. J. Wood, A. Piasecki, S. Kidder, M. N. Ducea, and K. A. Farley (2012), Late Cretaceous gravitational collapse of the southern Sierra Nevada batholith, California, *Geosphere*, *8*(2), 314–341.

Chernak, L. J., G. Hirth, J. Selverstone, and J. Tullis (2009), Effect of aqueous and carbonic fluids on the dislocation creep strength of quartz, *J. Geophys. Res.*, *114*, B04201, doi:10.1029/2008JB005884.

Christiansen, P. P. (1995), Faulting and hydrothermal processes in a granitic batholith, PhD thesis, 250 pp, Stanford Univ., Stanford, Calif.

Christiansen, P. P., and D. D. Pollard (1997), Nucleation, growth and structural development of mylonitic shear zones in granitic rock, *J. Struct. Geol.*, *19*(9), 1159–1172.

Christiansen, P. P., and D. D. Pollard (1998), Nucleation, growth and structural development of mylonitic shear zones in granitic rocks: Reply, *J. Struct. Geol.*, *20*(12), 1801–1803.

Coney, P. J., and S. J. Reynolds (1977), Cordilleran Benioff zones, *Nature*, *270*(5636), 403–406.

Cross, A. J., S. Kidder, and D. J. Prior (2015), Using microstructures and TitaniQ thermobarometry of quartz sheared around garnet porphyroclasts to evaluate microstructural evolution and constrain an Alpine Fault Zone geotherm, *J. Struct. Geol.*, *75*, 17–31.

Davies, R. K., and D. D. Pollard (1986), Relations between left-lateral strike-slip faults and right-lateral monoclinal kink bands in granodiorite, Mt Abbot Quadrangle, Sierra Nevada, California, *Pure Appl. Geophys.*, *124*(1–2), 177–201.

Davis, J. W., D. S. Coleman, J. T. Gracely, R. Gaschnig, and M. Stearns (2012), Magma accumulation rates and thermal histories of plutons of the Sierra Nevada batholith, CA, *Contrib. Mineral. Petrol.*, *163*(3), 449–465.

Delaney, P. T. (1987), Heat transfer during emplacement and cooling of mafic dykes, *Mafic Dyke Swarms*, *34*, 31–46.

Di Toro, G., and G. Pennacchioni (2004), Superheated friction-induced melts in zoned pseudotachylytes within the Adamello tonalites (Italian Southern Alps), *J. Struct. Geol.*, *26*(10), 1783–1801.

Dickinson, W. R., and W. S. Snyder (1978), Plate tectonics of the Laramide orogeny, in *Laramide Folding Associated with Basement Block Faulting in the Western United States*, edited by V. Matthews, pp. 355–366, The Geological Society of America, Inc., Boulder, Colo.

Ducea, M., and J. Saleeby (1998), A case for delamination of the deep batholithic crust beneath the Sierra Nevada, California, *Int. Geol. Rev.*, *40*(1), 78–93.
Dumitru, T. A. (1990), Subnormal Cenozoic geothermal gradients in the extinct Sierra Nevada magmatic arc: Consequences of Laramide and Post-Laramide shallow-angle subduction, *J. Geophys. Res.*, *95*(B4), 4925–4941.
Dumitru, T. A., P. B. Gans, D. A. Foster, and E. L. Miller (1991), Refrigeration of the western Cordilleran lithosphere during Laramide shallow-angle subduction, *Geology*, *19*(11), 1145–1148.
Durham, W. B., V. V. Mirkovich, and H. C. Heard (1987), Thermal-diffusivity of igneous rocks at elevated pressure and temperature, *J. Geophys. Res.*, *92*(B11), 11,615–11,634.
Engebretson, D. C., A. Cox, and R. G. Gordon (1985), Relative motions between oceanic and continental plates in the Pacific basin, *Spec. Pap.– Geol. Soc. Am.*, *206*, 1–60.
Evernden, J. F., and R. W. Kistler (1970), Chronology of emplacement of Mesozoic batholithic complexes in California and western Nevada, *U.S. Geol. Surv. Prof. Pap.*, *623*, 1–42.
Fyfe, W. S. (1973), Generation of batholiths, *Tectonophysics*, *17*(3), 273–283.
Ghent, E. D., and M. Z. Stout (1984), TiO2 activity in metamorphosed pelitic and basic rocks: Principles and applications to metamorphism in southeastern Canadian Cordillera, *Contrib. Mineral. Petrol.*, *86*(3), 248–255.
Green, D., and R. Schweickert (1995), The Gem Lake shear zone: Cretaceous dextral transpression in the northern Ritter Range pendant, eastern Sierra Nevada, California, *Tectonics*, *14*(4), 945–961.
Griffith, W. A., G. Di Toro, G. Pennacchioni, and D. D. Pollard (2008), Thin pseudotachylytes in faults of the Mt. Abbot quadrangle, Sierra Nevada: Physical constraints for small seismic slip events, *J. Struct. Geol.*, *30*(9), 1086–1094.
Griffith, W. A., P. F. Sanz, and D. D. Pollard (2009a), Influence of outcrop scale fractures on the effective stiffness of fault damage zone rocks, *Pure Appl. Geophys.*, *166*(10-11), 1595–1627.
Griffith, W. A., G. Di Toro, G. Pennacchioni, D. D. Pollard, and S. Nielsen (2009b), Static stress drop associated with brittle slip events on exhumed faults, *J. Geophys. Res.*, *114*, B02402, doi:10.1029/2008JB005879.
Grove, M., and T. M. Harrison (1996), Ar-40* diffusion in Fe-rich biotite, *American Mineralogist*, *81*(7-8), 940–951.
Grujic, D., M. Stipp, and J. L. Wooden (2011), Thermometry of quartz mylonites: Importance of dynamic recrystallization on Ti-in-quartz reequilibration, *Geochem. Geophys. Geosyst.*, *12*, Q06012, doi:10.1029/2010GC003368.
Guermani, A., and G. Pennacchioni (1998), Brittle precursors of plastic deformation in a granite: An example from the Mont Blanc massif (Helvetic, western Alps), *J. Struct. Geol.*, *20*(2-3), 135–148.
Hames, W. E., and S. A. Bowring (1994), An empirical evaluation of the argon diffusion geometry in muscovite, *Earth Planet. Sci. Lett.*, *124*(1–4), 161–167.
Hansen, L. N., M. J. Cheadle, B. E. John, S. M. Swapp, H. J. Dick, B. E. Tucholke, and M. A. Tivey (2013), Mylonitic deformation at the Kane oceanic core complex: Implications for the rheological behavior of oceanic detachment faults, *Geochem. Geophys. Geosyst.*, *14*, 3085–3108, doi:10.1002/ggge.20184.
Hanson, R. B., and M. D. Barton (1989), Thermal development of low-pressure metamorphic belts: Results from two-dimensional numerical models, *J. Geophys. Res.*, *94*(B8), 10,363–10,377.
Harrison, T. M. (1981), Diffusion of Ar-40 in hornblende, *Contrib. Mineral. Petrol.*, *78*(3), 324–331.
Harrison, T. M., and G. K. C. Clarke (1979), Model of the thermal effects of igneous intrusion and uplift as applied to Quottoon pluton, British Columbia, *Can. J. Earth Sci.*, *16*(3), 411–420.
Harrison, T. M., I. Duncan, and I. Mcdougall (1985), Diffusion of Ar-40 in biotite: Temperature, pressure and compositional effects, *Geochim. Cosmochim. Acta*, *49*(11), 2461–2468.
Hayden, L. A., and E. B. Watson (2007), Rutile saturation in hydrous siliceous melts and its bearing on Ti-thermometry of quartz and zircon, *Earth Planet. Sci. Lett.*, *258*(3-4), 561–568.
Hirth, G., and J. Tullis (1992), Dislocation creep regimes in quartz aggregates, *J. Struct. Geol.*, *14*(2), 145–159.
Huang, R. F., and A. Audétat (2012), The titanium-in-quartz (TitaniQ) thermobarometer: A critical examination and re-calibration, *Geochim. Cosmochim. Acta*, *84*, 75–89.
Jaeger, J. C. (1964), Thermal effects of intrusions, *Rev. Geophys.*, *2*(3), 443–466.
Johnson, B. W. (2009), Oxygen isotope, cathodoluminescence, and titanium in quartz geothermometry in the Alta Stock, UT: Geochemical insights into pluton assembly and early cooling history, MS thesis, 83 pp., Univ. of Utah, Salt Lake City, UT.
Kidder, S., J. P. Avouac, and Y. C. Chan (2013), Application of titanium-in-quartz thermobarometry to greenschist facies veins and recrystallized quartzites in the Hsuehshan range, Taiwan, *Solid Earth*, *4*(1), 1–21.
Kidder, S., G. Hirth, J. P. Avouac, and W. Behr (2016), The influence of stress history on the grain size and microstructure of experimentally deformed quartzite, *J. Struct. Geol.*, *83*, 194–206.
Kirkpatrick, J. D., and Z. K. Shipton (2009), Geologic evidence for multiple slip weakening mechanisms during seismic slip in crystalline rock, *J. Geophys. Res.*, *114*, B12401, doi:10.1029/2008JB006037.
Kirkpatrick, J. D., Z. K. Shipton, and C. Persano (2009), Pseudotachylytes: Rarely generated, rarely preserved, or rarely reported?, *Bull. Seismol. Soc. Am.*, *99*(1), 382–388.
Kirkpatrick, J. D., Z. K. Shipton, J. P. Evans, S. Micklethwaite, S. J. Lim, and P. McKillop (2008), Strike-slip fault terminations at seismogenic depths: The structure and kinematics of the Glacier Lakes fault, Sierra Nevada United States, *J. Geophys. Res.*, *113*, B04304, doi:10.1029/2007JB005311.
Kohn, M. J., and C. J. Northrup (2009), Taking mylonites' temperatures, *Geology*, *37*(1), 47–50.
Kronenberg, A. K., P. Segall, and G. H. Wolf (1990), Hydrolytic weakening and penetrative deformation within a natural shear zone, *Geophys. Monogr.*, *56*, 21–36.
Lee, J. K. W., I. S. Williams, and D. J. Ellis (1997), Pb, U and Th diffusion in natural zircon, *Nature*, *390*(6656), 159–162.
Lister, G. S., and A. W. Snoke (1984), S-C mylonites, *J. Struct. Geol.*, *6*(6), 617–638.
Lloyd, G. E., and B. Freeman (1994), Dynamic recrystallization of quartz under greenschist conditions, *J. Struct. Geol.*, *16*(6), 867–881.
Lockwood, J. P., and P. A. Lydon (1975), Geologic map of the Mount Abbot Quadrangle, central Sierra Nevada, *U.S. Geol. Surv. Geol. Quatangle*, 1155, scale 62500.
Lovering, T. S. (1935), Theory of heat conduction applied to geological problems, *Bull. Geol. Soc. Am.*, *46*(1/4), 69–94.
Lovering, T. S. (1936), Heat conduction in dissimilar rocks and the use of thermal models, *Bull. Geol. Soc. Am.*, *47*(1/4), 87–U29.
Maaløe, S., and P. J. Wyllie (1975), Water content of a granite magma deduced from the sequence of crystallization determined experimentally with water-undersaturated conditions, *Contrib. Mineral. Petrol.*, *52*(3), 175–191.

MacDonald, W. D., J. J. Estrada, G. M. Sierra, and H. Gonzalez (1996), Late Cenozoic tectonics and paleomagnetism of North Cauca Basin intrusions, Colombian Andes: Dual rotation modes, *Tectonophysics*, *261*(4), 277–289.
Mahon, K. I., T. M. Harrison, and D. A. Drew (1988), Ascent of a granitoid diapir in a temperature varying medium, *J. Geophys. Res.*, *93*(B2), 1174–1188.
Mancktelow, N. S., and G. Pennacchioni (2005), The control of precursor brittle fracture and fluid–rock interaction on the development of single and paired ductile shear zones, *J. Struct. Geol.*, *27*(4), 645–661.
Mansfield, C. F. (1979), Upper Mesozoic subsea fan deposits in the southern Diablo Range, California: Record of the Sierra Nevada magmatic arc, *Geol. Soc. Am. Bull.*, *90*(11), 1025–1046.
Martel, S. J. (1999), Mechanical controls on fault geometry, *J. Struct. Geol.*, *21*(6), 585–596.
Martel, S. J. (1990), Formation of compound strike-slip fault zones, Mount Abbot Quadrangle, California, *J. Struct. Geol.*, *12*(7), 869–877.
Martel, S. J., and D. D. Pollard (1989), Mechanics of slip and fracture along small faults and simple strike-slip fault zones in granitic rock, *J. Geophys. Res.*, *94*(B7), 9417–9428.
Martel, S. J., D. D. Pollard, and P. Segall (1988), Development of simple strike-slip fault zones, Mount Abbot Quadrangle, Sierra Nevada, California, *Geol. Soc. Am. Bull.*, *100*(9), 1451–1465.
Mel'nikova, N. V., V. V. Rzhevskogo, and M. M. Protod'yakonova (1975), *Spravochnik (Kadastr) Fisicheskikh Svoystv Gornykh Porod (Handbook [Registry] of Physical Properties of Rocks)*, 279 pp., Nedra, Moscow.
Menegon, L., and G. Pennacchioni (2010), Local shear zone pattern and bulk deformation in the Gran Paradiso metagranite (NW Italian Alps), *Int. J. Earth Sci.*, *99*(8), 1805–1825.
Moore, J. G. (1963), Geology of the Mount Pinchot quadrangle, southern Sierra Nevada, California, *U.S. Geol. Surv. Bull.*, *1301*, 152 p.
Morgan, D. J., M. C. Jollands, G. E. Lloyd, and D. A. Banks (2014), Using titanium-in-quartz geothermometry and geospeedometry to recover temperatures in the aureole of the Ballachulish Igneous Complex, NW Scotland, in *Deformation Structures and Processes within the Continental Crust*, edited by S. Llana-Fúnez, A. Marcos and F. Bastida, pp. 145–165, Geol. Soc., London.
Morgan, P. (1984), The thermal structure and thermal evolution of the continental lithosphere, *Phys. Chem. Earth*, 15, 107–193.
Morrow, C. A., and D. A. Lockner (2006), Physical properties of two core samples from well 34-9RD2 at the Coso Geothermal Field, California, *U.S. Geol. Surv. Open File Rep.*, *2006-1230*, 1–32.
Nabelek, P. I., A. M. Hofmeister, and A. G. Whittington (2012), The influence of temperature-dependent thermal diffusivity on the conductive cooling rates of plutons and temperature-time paths in contact aureoles, *Earth Planet. Sci. Lett.*, *317*, 157–164.
Nachlas, W. O., and G. Hirth (2015), Experimental constraints on the role of dynamic recrystallization on resetting the Ti-in-quartz thermobarometer, *J. Geophys. Res. Solid Earth*, *120*, 8120–8137, doi:10.1002/2015JB012274.
Nachlas, W. O., D. L. Whitney, C. Teyssier, B. Bagley, and A. Mulch (2014), Titanium concentration in quartz as a record of multiple deformation mechanisms in an extensional shear zone, *Geochem. Geophys. Geosyst.*, *15*, 1374–1397.
Nadin, E. S. (2007), Structure and history of the Kern Canyon fault system, southern Sierra Nevada, California, PhD thesis, 296 pp, Calif. Inst. of Technol., Pasadena.
Nadin, E. S., and J. B. Saleeby (2008), Disruption of regional primary structure of the Sierra Nevada batholith by the Kern Canyon fault system, California, in *Ophiolites, Arcs, and Batholiths: A Tribute to Cliff Hopson*, edited by J. E. Wright and J. W. Shervais, Spec. Pap. Geo. Soc. Am., 438, 429–454.
Nadin, E. S., J. Saleeby, and M. Wong (2016), Thermal evolution of the Sierra Nevada batholith, California, and implications for strain localization, *Geosphere*, *12*(2), 377–399.
Nevitt, J. M. (2015), *Fault-Related Deformation Within the Brittle-Ductile Transition: Field Observations, Microstructural Analysis, and Mechanical Modeling*, 257 pp., Stanford University, Stanford, Calif.
Nevitt, J. M., and D. D. Pollard (2017), Impacts of off-fault plasticity on fault slip and interaction at the base of the seismogenic zone, *Geophys. Res. Lett.*, *44*, doi:10.1002/2016GL071688.
Nevitt, J. M., D. D. Pollard, and J. M. Warren (2014), Evaluation of transtension and transpression within contractional fault steps: Comparing kinematic and mechanical models to field data, *J. Struct. Geol.*, *60*, 55–69.
Norton, D., and J. Knight (1977), Transport phenomena in hydrothermal Systems: Cooling plutons, *Am. J. Sci.*, *277*(8), 937–981.
Nyman, M. W., R. D. Law, and E. A. Smelik (1992), Cataclastic deformation mechanism for the development of core-mantle structures in amphibole, *Geology*, *20*(5), 455–458.
Pachell, M. A., and J. P. Evans (2002), Growth, linkage, and termination processes of a 10-km-long strike-slip fault in jointed granite: The Gemini fault zone, Sierra Nevada, California, *J. Struct. Geol.*, *24*(12), 1903–1924.
Pachell, M. A., J. P. Evans, and W. L. Taylor (2003), Kilometer-scale kinking of crystalline rocks in a transpressive convergent setting, Central Sierra Nevada, California, *Geol. Soc. Am. Bull.*, *115*(7), 817–831.
Passchier, C. W., and R. A. J. Trouw (2006), *Microtectonics*, 2 ed., Springer, Berlin.
Peacock, S. M. (1989), Thermal modeling of metamorphic pressure-temperature-time paths: A forward approach, in *Metamorphic Pressure-Temperature-Time Paths*, edited by F. S. Spear and S. M. Peacock, pp. 57–102, AGU, Washington, D. C.
Pennacchioni, G. (2005), Control of the geometry of precursor brittle structures on the type of ductile shear zone in the Adamello tonalites, Southern Alps (Italy), *J. Struct. Geol.*, *27*(4), 627–644.
Pennacchioni, G., and N. S. Mancktelow (2007), Nucleation and initial growth of a shear zone network within compositionally and structurally heterogeneous granitoids under amphibolite facies conditions, *J. Struct. Geol.*, *29*(11), 1757–1780.
Pennacchioni, G., and N. S. Mancktelow (2013), Initiation and growth of strike-slip faults within intact metagranitoid (Neves area, eastern Alps, Italy), *Geol. Soc. Am. Bull.*, *125*(9-10), 1468–1483.
Pennacchioni, G., and E. Zucchi (2013), High temperature fracturing and ductile deformation during cooling of a pluton: The Lake Edison granodiorite (Sierra Nevada batholith, California), *J. Struct. Geol.*, *50*, 54–81.
Pollard, D. D., and R. C. Fletcher (2005), *Fundamentals of Structural Geology*, 500 pp., Cambridge Univ. Press, Cambridge, U. K.
Pryer, L. L. (1993), Microstructures in feldspars from a major crustal thrust zone: The Grenville Front, Ontario, Canada, *J. Struct. Geol.*, *15*(1), 21–36.
Pryer, L. L., and P. Y. F. Robin (1995), Retrograde metamorphic reactions in deforming granites and the origin of flame perthite, *J. Metamorph. Geol.*, *13*(6), 645–658.
Ramsay, J. G. (1967), *Folding and Fracturing of Rocks*, 568 pp., McGraw-Hill, New York.
Renne, P. R., O. T. Tobisch, and J. B. Saleeby (1993), Thermochronological record of pluton emplacement, deformation, and exhumation at Courtright shear zone, Central Sierra Nevada, California, *Geology*, *21*(4), 331–334.
Riklin, K. (1983), Contact metamorphism of the Permian red sandstones in the Adamello area, *Mem. Soc. Geol. Ital.*, *26*, 159–169.
Ritz, E., D. D. Pollard, and M. Ferris (2015), The influence of fault geometry on small strike-slip fault mechanics, *J. Struct. Geol.*, *73*, 49–63.

Schmid, S. M., and M. Casey (1986), Complete fabric analysis of some commonly observed quartz c-axis patterns, in *Mineral and Rock Deformation: Laboratory Studies: The Patterson Volume*, edited by B. E. Hobbs and H. C. Heard, pp. 246–261, AGU, Washington, D. C.

Schofield, D. I., and R. S. D'Lemos (1998), Relationships between syn-tectonic granite fabrics and regional PTtd paths: An example from the Gander-Avalon boundary of NE Newfoundland, *J. Struct. Geol.*, *20*(4), 459–471.

Segall, P., and D. D. Pollard (1980), Mechanics of discontinuous faults, *J. Geophys. Res.*, *85*(Nb8), 4337–4350.

Segall, P., and D. D. Pollard (1983a), Joint formation in granitic rock of the Sierra Nevada, *Geol. Soc. Am. Bull.*, *94*(5), 563–575.

Segall, P., and D. D. Pollard (1983b), Nucleation and growth of strike slip faults in granite, *J. Geophys. Res.*, *88*(B1), 555–568.

Segall, P., and C. Simpson (1986), Nucleation of ductile shear zones on dilatant fractures, *Geology*, *14*(1), 56–59.

Segall, P., E. H. Mckee, S. J. Martel, and B. D. Turrin (1990), Late Cretaceous age of fractures in the Sierra Nevada batholith, California, *Geology*, *18*(12), 1248–1251.

Shaw, C. A., L. W. Snee, J. Selverstone, and J. C. Reed (1999), Ar-40/Ar-39 thermochronology of mesoproterozoic metamorphism in the Colorado front range, *J. Geol.*, *107*(1), 49–67.

Shigematsu, N. (1999), Dynamic recrystallization in deformed plagioclase during progressive shear deformation, *Tectonophysics*, *305*(4), 437–452.

Simpson, C., and R. P. Wintsch (1989), Evidence for deformation-induced K-feldspar replacement by myrmekite, *J. Metamorph. Geol.*, *7*(2), 261–275.

Spera, F. A. (1980), Aspects of magma transport, in *Physics of Magmatic Processes*, edited by R. B. Hargraves, pp. 265–323, Princeton Univ. Press, Princeton, N. J.

Stern, T. W., P. C. Bateman, B. A. Morgan, M. F. Newall, and D. L. Peck (1981), Isotopic U-Pb ages of zircon from the granitoids of the central Sierra Nevada, California, *U.S. Geol. Surv. Prof. Pap.*, *1185*, 17 p.

Stesky, R., W. Brace, D. Riley, and P.-Y. Robin (1974), Friction in faulted rock at high temperature and pressure, *Tectonophysics*, *23*(1), 177–203.

Stesky, R. M. (1978), Mechanisms of high-temperature frictional sliding in Westerly granite, *Can. J. Earth Sci.*, *15*(3), 361–375.

Stipp, M., H. Stünitz, R. Heilbronner, and S. M. Schmid (2002), The eastern Tonale fault zone: A 'natural laboratory' for crystal plastic deformation of quartz over a temperature range from 250 to 700 degrees C, *J. Struct. Geol.*, *24*(12), 1861–1884.

Stowell, H. H., and M. A. Pike (2000), One-dimensional thermal models of metamorphism resulting from the Coast Plutonic Complex sill, nothern Coast Mountains, southeastern Alaska, in *Tectonics of the Coast Mountains, Southeastern Alaska and British Columbia*, edited by H. H. Stowell and W. C. McClelland, Geol. Soc. of Am. Spec. Pap., Boulder, Colo.

Thomas, J. B., E. B. Watson, F. S. Spear, P. T. Shemella, S. K. Nayak, and A. Lanzirotti (2010), TitaniQ under pressure: The effect of pressure and temperature on the solubility of Ti in quartz, *Contrib. Mineral. Petrol.*, *160*(5), 743–759.

Thomas, J. B., E. B. Watson, F. S. Spear, and D. A. Wark (2015), TitaniQ recrystallized: Experimental confirmation of the original Ti-in-quartz calibrations, *Contrib. Mineral. Petrol.*, *169*, 27–43.

Tikoff, B. (1994), Transpression: Strain theory and application to the emplacement and deformation of granite, Sierra Nevada, CA, PhD thesis, Univ. of Minnesota, Minneapolis.

Tikoff, B., and C. Teyssier (1992), Crustal-scale, en echelon P-shear tensional bridges: A possible solution to the batholithic room problem, *Geology*, *20*(10), 927–930.

Tikoff, B., and C. Teyssier (1994), Strain and fabric analyses based on porphyroclast interaction, *J. Struct. Geol.*, *16*(4), 477–491.

Tikoff, B., and M. de Saint Blanquat (1997), Transpressional shearing and strike-slip partitioning in the Late Cretaceous Sierra Nevada magmatic arc, California, *Tectonics*, *16*(3), 442–459.

Tikoff, B., C. Teyssier, and M. De saint Blanquat (1998), Nucleation, growth and structural development of mylonitic shear zones in granitic rocks: Discussion, *J. Struct. Geol.*, *20*(12), 1795–1799.

Titus, S. J., R. Clark, and B. Tikoff (2005), Geologic and geophysical investigation of two fine-grained granites, Sierra Nevada Batholith, California: Evidence for structural controls on emplacement and volcanism, *Geol. Soc. Am. Bull.*, *117*(9-10), 1256–1271.

Tobisch, O. T., J. B. Saleeby, P. R. Renne, B. Mcnulty, and W. X. Tong (1995), Variations in deformation fields during development of a large-volume magmatic arc, central Sierra Nevada, California, *Geol. Soc. Am. Bull.*, *107*(2), 148–166.

Tourigny, G., and A. Tremblay (1997), Origin and incremental evolution of brittle/ductile shear zones in granitic rocks: Natural examples from the southern Abitibi Belt, Canada, *J. Struct. Geol.*, *19*(1), 15–27.

Toy, V. G., D. J. Prior, and R. J. Norris (2008), Quartz fabrics in the Alpine Fault mylonites: Influence of pre-existing preferred orientations on fabric development during progressive uplift, *J. Struct. Geol.*, *30*(5), 602–621.

Wagner, G. A., G. M. Reimer, and E. Jager (1977), Cooling ages derived by apatite fission-track, mica Rb-Sr and K-Ar dating: The uplift and cooling history of the Central Alps, 27 pp., Soc. Coop. Tipogr.

Wark, D. A., and E. B. Watson (2006), TitaniQ: A titanium-in-quartz geothermometer, *Contrib. Mineral. Petrol.*, *152*(6), 743–754.

Wark, D. A., W. Hildreth, F. S. Spear, D. J. Cherniak, and E. B. Watson (2007), Pre-eruption recharge of the Bishop magma system, *Geology*, *35*(3), 235–238.

Whittington, A. G., A. M. Hofmeister, and P. I. Nabelek (2009), Temperature-dependent thermal diffusivity of the Earth's crust and implications for magmatism, *Nature*, *458*(7236), 319–321.

Wiebe, R. A., D. A. Wark, and D. P. Hawkins (2007), Insights from quartz cathodoluminescence zoning into crystallization of the Vinalhaven granite, coastal Maine, *Contrib. Mineral. Petrol.*, *154*(4), 439–453.

Wood, D. J. (1997), *Geology of the Eastern Tehachapi Mountains and Late Cretaceous-Early Cenozoic Tectonics of the Southern Sierra Nevada Region, Kern County, California*, 287 pp., Calif. Inst. of Technol., Pasadena.

Xu, B., M. Grove, C. Q. Wang, L. F. Zhang, and S. W. Liu (2000), Ar-40/Ar-39 thermochronology from the northwestern Dabie Shan: Constraints on the evolution of Qinling-Dabie orogenic belt, east-central China, *Tectonophysics*, *322*(3-4), 279–301.